Preprint IN/45 ⑰ 531027
2001 118 339 76P

Revised for Journal of Geophysical Research., Sept., 2000, Accepted Oct. 31, 2000.

Chemistry-climate interactions in the GISS GCM. Part 1: Tropospheric chemistry model description and evaluation

Drew T. Shindell[1], J. Lee Grenfell[1], David Rind[1], Colin Price[2], and Volker Grewe[1,3]

1 NASA Goddard Institute for Space Studies and Center for Climate Systems Research, Columbia University, New York, New York
2 Department of Geophysics and Planetary Sciences, Tel Aviv University, Ramat Aviv, Israel
3 DLR Institut fur Physik der Atmosphare, Oberpfaffenhofen, Germany

Abstract. A tropospheric chemistry module has been developed for use within the Goddard Institute for Space Studies (GISS) general circulation model (GCM) to study interactions between chemistry and climate change. The model uses a simplified chemistry scheme based on CO-NO_x-HO_x-O_x-CH_4 chemistry, and also includes a parameterization for emissions of isoprene, the most important non-methane hydrocarbon. The model reproduces present day annual cycles and mean distributions of key trace gases fairly well, based on extensive comparisons with available observations. Examining the simulated change between present day and pre-industrial conditions, we find that the model has a similar response to that seen in other simulations. It shows a 45% increase in the global tropospheric ozone burden, within the 25% - 57% range seen in other studies. Annual average zonal mean ozone increases by more than 125% at Northern Hemisphere middle latitudes near the surface. Comparison of model runs that allow the calculated ozone to interact with the GCM's radiation and meteorology with those that do not shows only minor differences for ozone. The common usage of ozone fields that are not calculated interactively seems to be adequate to simulate both the present day and the pre-industrial ozone distributions. However, use of coupled chemistry does alter the change in tropospheric oxidation capacity, enlarging the overall decrease in OH concentrations from the pre-industrial to the present by about 10% (-5.3% global annual average in uncoupled mode, -5.9% in coupled mode). This indicates that there may be systematic biases in the simulation of the pre-industrial to present day decrease in the oxidation capacity of the troposphere (though a ten percent difference is well within the total uncertainty). Global annual average radiative forcing from pre-industrial to present day ozone change is 0.32 W/m^2. The forcing seems to be increased by about 10% when the chemistry is coupled to the GCM. Forcing values greater than 0.8 W/m^2 are seen over large areas of the United States, Southern Europe, North Africa, the Middle East, Central Asia, and the Arctic. Radiative forcing is greater than 1.5 W/m^2 over parts of these areas during Northern summer. Though there are local differences, the radiative forcing is overall in good agreement with the results of other modeling studies in both its magnitude and spatial distribution, demonstrating that the simplified chemistry is adequate for climate studies.

1. Introduction

The buildup of both greenhouse gases and ozone precursors in the Earth's atmosphere due to anthropogenic emissions is well documented (e.g. IPCC, 1996). Since pre-industrial times, carbon dioxide has increased by ~30%, methane by about 150%, and NO_x is thought to have more than doubled. Just since the 1950s, carbon monoxide levels have increased by 50% at Northern Hemisphere mid-latitudes. The direct radiative influence of the well-mixed greenhouse gases has been studied intensely, and is now considered to be one of the lesser sources of uncertainty for recent climate change (e.g. Hansen et al., 1998). Induced changes in chemistry are much less clear. These changes have an indirect radiative effect by chemically altering the abundance of radiatively absorbing species such as ozone and methane.

The major chemical impacts of increasing emissions of greenhouse gases and ozone precursor gases such as nitrogen oxides (NO_x) are to produce tropospheric ozone, and to alter tropospheric

OH (which, along with ozone, largely governs the oxidation capacity of the troposphere). Ozone production requires NO_2 photolysis to create atomic oxygen, which then combines with molecular oxygen to form ozone, and hydrocarbons or carbon monoxide to turn OH into HO_2, which is necessary to allow the regeneration of NO_2 from the photolysis product NO. As ozone precursor gases have increased, enhanced tropospheric ozone abundances have resulted. In Northern Hemisphere industrial areas, surface ozone has doubled since the 1930s, while the entire tropospheric ozone column has increased by 20% over Europe just in the 1980s. Recent work indicates that tropospheric ozone changes may have accounted for a radiative forcing of up to ~1 W/m^2, which is roughly 30% of the total forcing due to greenhouse gases (Portmann et al., 1997). The amount of OH is reduced by the presence of greater levels of methane and carbon monoxide in the atmosphere, which alter the partitioning among hydrogen oxides (HO_x), favoring HO_2 over OH. While these changes are partially offset by the effects of increased NOx, ozone, water vapor, and temperature, all of which tend to increase the abundance of OH, the net effect of changes over the past 150 years seems to have been a decrease in OH concentration. This reduction of the tropospheric oxidation capacity acts as an important climate feedback, since oxidation via OH is the primary removal mechanism for tropospheric methane and carbon monoxide.

It is therefore necessary to include future levels of ozone precursors along with atmospheric chemistry in order to simulate future abundances of the greenhouse gases methane and ozone. Given the enormous computation costs of running a large climate model with interactive chemistry, we have chosen to develop a simplified scheme based on current understanding of the most important chemical processes in the troposphere. The clear advantage of using a simplified chemistry scheme is that the rapid computational speed allows for longer simulations to be run, permitting the model's variability to be accurately assessed, and for numerous sensitivity experiments to be performed, which is crucial to unraveling the complex interlinkages involved in chemistry-climate coupling. We present here detailed documentation of our simplified tropospheric chemistry model. Its performance is then evaluated based on comparison with observations for the present day, and its sensitivity to a commonly modeled perturbation is compared with other models. The model will be applied to sensitivity studies of chemistry and climate interactions in a follow-up paper (Grenfell et al., hereafter referred to as Part II), and has been applied to a study of upper tropospheric nitrogen oxides and ozone in Grewe et al. (2000).

2. Model Description

2.1 Chemistry

It is computationally very expensive to model the full range of chemical reactions in the troposphere in a GCM suitable for climate studies. Therefore we have chosen to use a subset of molecules, and include only the photochemical reactions that involve those chosen species. It is now accepted that the abundance of ozone is most often limited by the availability of NO_x, rather than the hydrocarbons which are also ozone precursors (e.g. Trainer et al., 1993; National Academy of Sciences panel on Air Quality Standards, 1996). Therefore, we have not included an explicit representation of non-methane hydrocarbons (NMHCs) in our reduced chemistry scheme. We do, however, include equivalent carbon monoxide emissions from isoprene, which is thought to be the most important contribution of NMHCs (Wang et al., 1998c; Horowitz et al., 1998).

The simplified chemistry scheme is based on CH_4, CO, NO_x ($NO + NO_2 + NO_3$ +HONO), HO_x (OH, HO_2), and O_x ($O+O(^1D)+O_3$) chemistry. Methane is set to fixed values in the troposphere, with 1.80 parts per million by volume (ppmv) in the Northern hemisphere and 1.70 ppmv in the Southern Hemisphere for the present day simulations (early 1990s values). Use of the chemical family approach, whereby radical species in particular 'families' (e.g. odd oxygen) are grouped together, and the reactions between family members are assumed to be rapid enough to maintain an equilibrium partitioning between individual family members at all times, yields a great computational time savings. We are then able to treat the family as a single species for transport.

Combined with the reduced chemistry set, we are able to use relatively few chemical tracers. The number of online tracers is an important factor in these simulations, as they are transported by a quadratic upstream scheme (Prather, 1986), which is very accurate (saving second order moments in all directions), but also very time consuming. Having few tracers allows the model to run much faster, and is a further motivation to use simplified chemistry. Ten chemical species are transported in the model: O_x , NO_x , H_2O_2, H_2O, CO, HNO_3, N_2O_5, HO_2NO_2, CH_3OOH, and HCHO. This is a significant savings over transporting all 24 molecules used in the simulations. After combining the short-lived radicals into equilibrated families, we find that all the species have long enough lifetimes (except for HOx, whose very short lifetime keeps it in equilibrium at all times) that we can use an extremely simple explicit scheme to calculate chemical changes, using a chemical time step of one hour. The chemistry scheme adds ~56% to the running time of the GCM, with 38% from chemistry and 18% from tracer transport.

The chemical scheme includes 52 reactions. Gas-phase and heterogeneous chemical reactions are given in Table 1. Heterogeneous hydrolysis of N_2O_5 into HNO_3 takes place on sulfate aerosols, using the reaction rate coefficients given in Dentener and Crutzen (1993). Sulfate surface areas are taken from an online calculation also performed with the GISS GCM (Koch et al., 1999), assuming a monodispersed size distribution. This is not entirely self-consistent as meteorology, and therefore clouds, changes from run to run, which would affect sulfate. In the future, we will attempt to couple the simulations of ozone and sulfate chemistry. Both may be affected, as the sulfate simulation relies on fixed fields of radical species, much as the ozone simulation presented here relies on a fixed sulfate distribution. The heterogeneous reaction on sulfate is critical to the model's ability to properly simulate the partitioning of nitrogen species in the dark.

Photolysis rates are calculated with Fast-J, a scheme which uses only seven wavelength intervals, yet deviates only slightly from a full line-by-line calculation (M. Prather, personal communication, 1999) and compares well with other photolysis schemes (Olson et al., 1997). The photolysis reactions included in the model are listed in Table 2. Photolysis calculations are performed every two hours, giving us a fairly realistic diurnal simulation.

2.2 Sources and Sinks

Emission inventories of NOx and CO have been compiled for the 4 × 5 degree latitude by longitude grid used in this model. The use of detailed NO_x and CO emissions is critical since emissions vary widely with location. Nitrogen oxide sources are quite similar to those specified for the NASA Subsonic Assessment (SASS) aircraft project, consisting of annual emissions from fossil fuel burning (22.6 Tg N yr^{-1}) taken from the Global Emission Inventory Activity (GEIA) data set (Benkovitz et al., 1996), and monthly emissions from biomass burning (5.3 Tg N yr^{-1}) from GEIA (Laursen et al., 1992), soils (5.9 Tg N yr^{-1}) from Müller (1992), and aircraft (0.6 Tg N yr^{-1}) from Baughcum (1996), as in Friedl (1997) and references therein (Table 3). CO emissions from energy use (520 Tg CO yr^{-1}) and from biomass burning (510 Tg CO yr^{-1}) are as in Wang et al. (1998a). An additional CO source is the conversion of isoprene emissions (yielding 145 Tg CO yr^{-1}), based on 590 Tg C yr^{-1} emission in isoprene as calculated in Wang et al. (1998a) as a function of temperature, vegetation type, leaf area index, and solar radiation, and then assuming an 11% conversion to carbon monoxide per molecule carbon (this value is quite uncertain, and may depend upon various factors including NOx abundances (see e.g. Horowitz et al., 1998). Emissions are from data sets for as close to 1990 as available, in practice ranging from 1985 to 1992. This period corresponds well with the data used to evaluate the model, which was predominantly taken during the 1980s and the early 1990s.

To model nitrogen oxides produced by lightning, the GISS convection scheme is first used to derive both the total lightning, and the cloud-to-ground lightning frequencies interactively in each grid box and at each timestep (Price et al., 1997). Then the production rate of NO_x from lightning is used to derive the NO_x produced, including a 'C-shaped' vertical distribution of the lightning produced NO_x (Pickering et al., 1998). Based on a comparison with the global lightning data set recently produced at NASA Marshall Space Flight Center (Boccippio et al., 1998; W. Koshak, personal communication, 2000), we revised our original parameterization of the lightning flash frequency to allow cloud overshooting events during very strong convective activity, primarily at Northern Hemisphere mid-latitudes. In practice, this allows lightning to be generated one level above the nominal cloud top height. The model now gives more lightning at mid-latitudes, improving the overall simulation of the global lightning frequency field (see Section 3.3).

Chemistry is only applied in the troposphere in this model (the lowest seven layers, up to ~140 mb). Stratospheric sources for ozone and NO_x are included. For ozone, we keep stratospheric amounts at the observed, seasonally varying levels used in the standard GISS model (Hansen et al., 1996), and then allow the model to transport ozone into the troposphere based on the existing gradients at each time step. NOx in the stratosphere is defined as a fraction of the ozone. This gives the basic structure of the observed NO_x distribution, with larger values at higher latitudes and smaller values in the tropics due to the Brewer-Dobson circulation. The result is a similar ratio in influx to the troposphere as both species have strong positive gradients with altitude around the tropopause. Though the coarse vertical resolution makes it difficult for the model to simulate cross-tropopause transport properly (Rind et al., 1999), and we plan to improve this in the future, using internally calculated fluxes does give us an internally consistent formulation that produces reasonable tropospheric ozone fields, and can also respond to perturbations. To examine the importance of a possible overestimate of transport of stratospheric ozone and NO_x to the troposphere, a sensitivity study was performed in which the stratospheric amounts were reduced by two-thirds.

Phase transformation and removal of soluble species is calculated using a wet deposition scheme as in Koch et al. (1999). Briefly, soluble gases can be removed into either moist convective plumes or large-scale clouds as derived from the GCM's internal cloud scheme (Del Genio and Yao, 1996). During convection, all chemical species are transported along with the convective plumes, with scavenging of soluble species within and below cloud updrafts. In large-scale stratiform clouds, soluble gases are removed based on the fraction of the grid-box over which precipitation is taking place. Washout of soluble species is calculated below precipitating clouds. In the case of either evaporation of precipitation before reaching the ground, or detrainment or evaporation from a convective updraft, the dissolved species are returned to the air.

Wet chemistry calculations take place in each grid box at each time step, including the coupling with the convection scheme's entraining and non-entraining plumes (which are based on the convective instability in the particular grid-box at that time), so are entirely consistent with the contemporaneous model physics. The solubility of each gas is determined by an effective Henry's Law coefficient, assuming a pH of 4.5. Surface dry deposition is calculated using a resistance-in-series model (Wesely and Hicks, 1977) coupled to a global, seasonally varying vegetation data set as in Chin et al. (1996). Note that the leaf area indices are therefore not connected with the GCM's land-surface component. Aerodynamic resistances are based on the model's surface heat and momentum fluxes, as in Koch et al. (1999).

2.3 Climate Model

The chemistry scheme has been installed directly into the latest version of the GISS climate model, II' (two-prime). This is a primitive equation model, run here with nine vertical layers, centered at 959, 894, 786, 634, 468, 321, 201, 103, and 26.5 mbars, and horizontal resolution of 4 × 5 degrees (latitude × longitude). The bottom seven layers are terrain following sigma levels, while the top two are constant pressure surfaces. The GCM's physics time step is one hour, so that changes to tracer masses from transport and chemistry are both applied every hour. Several improvements have been made in recent years which will influence chemistry through their effects on transport and moisture content (Hansen et al., 1983; 1996). The boundary layer parameterization has been recently revised, and now employs a finite modified Ekman layer with parameterizations for drag and mixing coefficients based on similarity theory, which impacts the vertical mixing of surface fluxes. Convection now includes entraining and non-entraining plumes, mass fluxes proportional to convective instability, explicit downdrafts, and the model contains a cloud liquid-water scheme, based on microphysical sources and sinks of cloud water, which carries both water and ice (DelGenio and Yao, 1996). The land surface parameterization has been greatly expanded, and now explicitly calculates transpiration, infiltration, soil water flow and runoff, all of which impact both water vapor and latent heat release to the atmosphere.

The capability of the GCM to model the transport of trace species accurately has also been greatly improved. All the chemical tracers, along with heat and moisture, are now advected using a quadratic upstream scheme (Prather, 1986). (Momentum advection uses a fourth-order scheme.) Additionally, improvements were made to the boundary layer and convection schemes (DelGenio et al., 1996). Improvements to transport both within the boundary layer and across the boundary layer edge, along with convection, are especially important, since trace gas emissions at the Earth's surface come from discrete, spatially inhomogeneous sources. A prime example of the improvements can be seen in the interhemispheric exchange times of CFC-11 and ^{85}Kr. In the earlier version of the model, the exchange times were roughly a factor of two too long, whereas in the new version, the values are within 15-25% of observations (Rind and Lerner, 1996). Improvements in the interhemispheric exchange time occurred because the alterations in both the boundary layer and convection schemes improved the tropical precipitation and wind fields. Interestingly, neither change by itself was overly effective, a result which illustrates the highly non-linear nature of GCM interactions. The GISS GCM II' has been used previously for ozone (Mickley et al., 1999) and sulfate (Koch et al., 1999) simulations.

The use of water vapor as an online, chemically active tracer is another important feature of this model. Most chemical models assume that water vapor is constant since they do not have a detailed model of the hydrological cycle, while most climate models do not have any chemistry. Thus the interaction between water vapor and climate through chemistry has seldom been examined, although it is thought to be an important issue in climate modeling (IPCC, 1996).

Calculated ozone fields are used in the GCM's computation of radiative heating and fluxes which is performed every five hours. These fully interactive chemical constituent changes are therefore able to affect the meteorology in the GCM. To explore the influence of this feedback, we have also performed simulations where this feedback was not allowed, in which case the model used a climatological ozone distribution in its radiation calculations. In addition to ozone, the GCM calculates radiative absorption and emission from water, CO_2, N_2O, chlorofluorocarbons and methane in the longwave, and CO_2, NO_2 and O_2 in the shortwave (Hansen et al., 1983). Changes in tropospheric ozone play an important role in the radiative heating that drives tropospheric meteorology, through their absorption in the Huggins bands in the ultraviolet, the Chappuis bands in the visible, and the 9.6 micron and especially the 14 micron bands in the infrared (Shine et al., 1995; van Dorland et al., 1997).

The simplified chemistry scheme adds only about 38% to the running time of the GCM, plus an additional ~18% for the transport of the chemical tracers. It is therefore computationally rapid enough that the GCM can be run with online chemistry for long-term climate simulations or for multiple runs to examine the sensitivity of the results to various changes. Although this model is certainly not as realistic as models containing more complete chemistry, it is able to reproduce the magnitude and variability (temporal, horizontal, and vertical) of important tropospheric trace gases on a global, three-dimensional basis, quite well, as detailed in section 3

3. Evaluation of Present-Day Simulation

Model simulations of present day conditions are taken from the last nine years of ten year runs (the model equilibrated during the first year), giving us good statistics on both the model's simulated mean values and its variability. These runs are evaluated by comparison with available tropospheric data sets. We focus primarily on ozone, due to its importance for climate modeling, and on its key precursors, CO and NOx (key in addition to methane, which is prescribed).

Additionally, we examine hydrogen peroxide, which plays an important role in both hydrogen oxide and sulfate chemistry, a topic we plan to explore in the future.

3.1 Ozone

Modeled annual cycles of ozone have been compared with the ozonesonde data climatology developed by Logan (1999). We compare several levels where the modeled and observed pressures are quite close, using measurements at 200, 300, 500, 800, and 950 mb compared with modeled values at 203, 323, 470, 787, and 959 mb, respectively. We will refer to these levels by the more standard pressure values of the data. Standard deviations of the model and as reported for the observations are both shown. However, it is difficult to ascertain how comparable the reported variability is to the simulated variability. The number of years of data varies from station to station and is not always very large, yielding varied quality in the derived interannual variability. Additionally, sampling biases (e.g. not flying balloons in bad weather) could also reduce the reported variability. On the model side, the large 4 x 5 degree grid box makes comparison with a single point quite difficult, and there could also be problems from numerical noise in the GCM's chemical or tracer transport schemes. We therefore concentrate on comparing the mean values, and focus less on the variability.

Figure 1 shows the results of these comparisons for a sampling of sites covering a wide range of the globe in latitude. At the uppermost model level which includes chemistry, centered at 200 mb, the model underestimates the seasonal cycle at middle and high latitudes in both hemispheres, failing to capture the late winter/springtime ozone maximum seen in observations. The very large values measured at these levels tag the ozone as originating in the stratosphere (a commonly used threshold for identifying air as being stratospheric in origin is 150 parts per billion by volume (ppbv), see e.g. Grewe et al., 2000). At polar latitudes, such as Resolute (75 N), this level is actually in the stratosphere during the late winter/spring season. This model is designed to simulate tropospheric chemistry only, so would not be expected to reproduce ozone values in stratospheric air. While a stratospheric ozone climatology is used in the model, the coarse vertical resolution of the model at these levels does not allow it to capture the seasonal motion of the tropopause accurately, nor to simulate stratosphere-troposphere exchange fully (Rind et al., 1996). The underestimation of middle and high latitude ozone at 200 mb is thus a GCM artifact, rather than a chemical shortcoming. During future model development, we will include the chemistry into a version of the GCM with higher vertical resolution in the tropopause region.

In the tropics and subtropics (Hilo at 20 N and Natal at 6 S in Figure 1, Pretoria at 26 S in Figure 2, and Samoa at 14 S which is not shown), the model does a reasonably good job of reproducing observed ozone amounts at 200 mb, though there is a slight positive bias. The model has only slightly more variability than seen in the observations.

In the middle troposphere from about 800 to 300 mb, the model reproduces both observed ozone abundances and the seasonal cycle fairly well. The model is able to capture the summer maximum seen at middle and high latitudes in the Northern Hemisphere. At 300 mb, both the mean values and the standard deviations in the model agree well with the observations. At lower levels, the model has more variability than is observed, even when its mean values agree quite well (e.g. Hohenpeissenberg at 500 mb). In the tropics and subtropics, the model reproduces fairly well the Feb-June maximum at Hilo, the Sep-Nov maximum at Natal, and the near lack of seasonality at Samoa (not shown). The variance of ozone values found in the model also agrees quite well with the measurements. In the Southern Hemisphere extratropics, the model again captures the minimal seasonality at both Lauder and Syowa. The standard deviations agree fairly well at 300 mb, but the model cannot reproduce the extremely small values reported for the observed standard deviations at 500 and 800 mb.

Surface ozone values are simulated quite well in the model. The primary exception is at Northern mid-latitudes, where the modeled summertime values are too large. It is difficult to compare a 4 by 5 degree grid box with observations at a single point however. In the case shown in

Figure 1, for Hohenpeissenberg, the model grid box which includes that relatively remote, unpolluted, hilltop site also includes many industrial cities in central Europe. At higher levels, where air has had more time to mix, this differential becomes less and less important, but at the surface it can be quite significant. Standard deviations of surface ozone mixing ratios appear to be overestimated in the model outside the tropics.

Figure 2 shows several ozone profile comparisons between observations and model values. Both the standard model run, and an alternate run with 60% less ozone in the stratosphere (which results in a 70% reduction in the flux of ozone from the stratosphere to the troposphere) are shown. In general, the standard simulation gives a fairly good reproduction of the observed profiles at most locations, with the simulated mean values lying within the standard deviation of the observations at all points except for Pretoria in January at upper levels, and Sapporo, where the model values are too small at high levels in January, and too large at the surface year round. Based on the sonde/model comparisons, it is difficult to determine which simulation is better. A prime example of this difficulty is shown in the Pretoria comparisons, where the run with reduced stratospheric ozone clearly gives a better match to the observations than the standard run in January, but the opposite is true in July. While the upper levels of the Natal comparisons suggest that a stratosphere-to-troposphere ozone flux somewhere in between the two cases shown here would be best, the Wallops Island and Sapporo comparisons show that both simulations tend to underpredict upper level ozone. This is especially true at Sapporo during winter, when the stratosphere-troposphere flux is largest at Northern mid-latitudes. While omission of NMHCs from the model has likely reduced ozone production above 300 mb by 0-20 % (Wang et al., 1998c), these results also indicate the importance of improving the representation of stratosphere-troposphere exchange processes in the GCM. Furthermore, the ozone profiles at Northern middle latitude are actually in excellent agreement with observations when compared relative to the tropopause height (Grewe et al., 2000). This suggests that much of the discrepancy shown in Figure 2 results from a poorly located model tropopause (typically too high at Northern middle latitudes) rather than a chemical bias. This will likely improve as we move to a model with higher vertical resolution. However, recent observations indicate that at high NO_x levels, current understanding of ozone chemistry in the upper troposphere may also have deficiencies (Jaegle et al., 1999). This may be improved by recent revisions to two relevant reaction rates that are not yet incorporated into the model (Brown et al., 1999; Portmann, 1999).

Near surface ozone (values at the center of the lowest layer) is shown in Figure 3. January values are distinctly less than July values over the Northern Hemisphere polluted continental regions, due to enhanced photochemical ozone formation in summer. Over the Southern Hemisphere continents, July values are also larger, primarily as a result of biomass burning. Values are larger over the continents in July, and in January for the Southern Hemisphere, but are larger over the oceans in January for the Northern Hemisphere (probably as a result of comparatively rapid continental deposition). These ozone distributions are fairly similar to those found in other models, though again there are large differences between model formulations. Sample comparisons are presented in Table 4. Most of the models agree fairly well over polluted areas such as the Eastern United States. The models also generally agree with observations from Wallops Island. Though located at a relatively remote site off the American coast, this site receives polluted air in the outflow from the interior. All of the models simulate a July maximum over south-west Africa, though some find values somewhat larger than those measured at Brazzaville. An interesting region is on the Antarctic coast near Syowa station, where many of the models are on the low side of the ozonesonde record. Since this region is far removed from most anthropogenic emissions, this may indicate problems with the basic chemistry or transport mechanisms used in these models. Similarly, several of the same models have lower values than observed over the relatively remote North Atlantic. The GISS model does a good job at all of these sites.

Large inter-model differences in the ozone budget (Table 5) are indicative of the large uncertainties remaining even after models are shown to reproduce the limited set of available observations. The net chemical ozone change, which is the difference between two large production and loss terms (~3500 Tg/yr each), varies from -810 to +550 Tg/yr. Our model lies within that range, and is near the high end of the range for both ozone removal by dry deposition and influx from the stratosphere. Recent satellite observations suggest that the stratosphere-to-troposphere flux is between 450 and 590 Tg per year (Gettelman et al., 1997), lower than the value seen in our model, as expected from tracer transport studies indicating that the 9-layer version of the GISS GCM has too much downward transport across the tropopause for the global, annual average (Rind et al., 1999). Since the abundance of ozone is a highly non-linear function of the amount of ozone precursors, small changes in precursor species can also significantly affect the ozone budget. The total tropospheric ozone burden of 262 Tg is again within the range seen in other models with more detailed chemistry. To calculate this value, we have summed over all grid boxes with 150 ppbv or less ozone, using this threshold to define tropospheric air. If we simply sum over the lowest seven levels, we find an ozone burden of 422 Tg. As the model has very coarse resolution in the tropopause region, it cannot accurately discriminate stratospheric ozone, and therefore using the 150 ppbv threshold is more realistic. Since there is little chemistry and no deposition in the top layers, the source and sink terms over that region are insignificantly altered from those calculated for the bottom seven layers. Though this model does not include NMHC chemistry, this has been shown to have a fairly small effect on the total ozone budget (Wang et al., 1998c), so has probably not greatly influenced these results. Furthermore, isoprene-generated carbon monoxide is included in the model, and isoprene accounts for about half of the overall effect of NMHCs (though some of these effects are via PAN, which is also not included here) (Wang et al., 1998c).

3.2 Carbon Monoxide

A comparison between the simulated annual cycle of carbon monoxide near the surface and observations (Novelli et al., 1998) is shown in Figure 4. While the model overestimates the seasonal variation at the high northern latitude site, it does a fairly good job of matching the abundances at other latitudes, where it obtains agreement with observations similar to other models (e.g. Mickley et al., 1999). As in the case of ozone, the model produces the best results in the tropics and at southern middle latitudes. Variability in the model may be overestimated, however. The standard deviation of the model results is typically 5 to 10 times larger than observed, but the observations covered periods of only 4 to 7 years, and either the observations or the simulations could be subject to many of the same problems as discussed in the previous section for ozone.

Few global data sets are available for tropospheric constituents. Carbon monoxide observations were taken by the Measurement of Air Pollution from Satellites (MAPS) experiment flown aboard the space shuttle (Connors et al., 1999). The instrument took measurements during October 1984, April 1994, and October 1994. Though short term, these measurements provide a useful comparison for a global model's distribution. Figure 5 shows carbon monoxide mixing ratios in the GCM and as observed by MAPS. The instrument samples the entire tropospheric column, with an averaging kernel centered at approximately 7-8 km altitude (Reichle et al., 1999), and the mean value is shown here. Model output has been weighted according to the same profile. The April comparison shows that the model does a fairly good job representing the overall meridional gradient in CO. The global average value is also accurately reproduced by the model. The largest values in the tropics and subtropics are in somewhat different locations, however. The model puts maxima over the continents, especially over Central America and East Africa. While the observations are relatively sparse, there seem to be larger values over the tropical Atlantic and over the Western Pacific than seen in the model. The latter would presumably result from a large Asian source, and may indicate that this source is underestimated in the GCM. The October comparison is more complex. The model shows very large CO values over South America, which also appear in the 1994 observations. However, the large values (greater than 120 ppbv) in the observations seem to extend over much of the Southern Hemisphere subtropics, while they are more confined to the continents in the GCM. The model is run with a compilation of emissions from 1985 through 1992, so that it seems sensible that it falls somewhere between the two observed periods. Interannual variability, though, makes it difficult to interpolate between the two individual years. For example, extremely large fires burned over Indonesia during 1994, making this an exceptional year for biomass burning emissions. Overall, the model appears to have a reasonable global distribution and magnitude in both seasons, though it generally underestimates CO due to the outflow of polluted continental air. In both April and October, the model also has a low bias at Southern Hemisphere middle latitudes.

3.3 Nitrogen Oxides and Lightning

Comparison of modeled NO_x in the middle and upper troposphere with measurements obtained as part of the Nitrogen OXides and ozone measurements along Air Routes (NOXAR) program is shown in Figure 6 (see Grewe et al., 2000 for a more detailed comparison). The model generally reproduces the observed mixing ratios quite well in the middle troposphere. It tends to underestimate nitrogen oxide abundances in the region from about 1 to 3 km below the tropopause, however, except during Northern Hemisphere summer. This may be a contributing factor to the underestimation of ozone at Northern Hemisphere mid-latitudes in this altitude range (Figures 1 and 2). At the altitude of the tropopause, the model overestimates NOx, except in Northern wintertime. The mean values shown in Figure 6 can be misleading, as Grewe et al. (2000) showed that the most frequent NO_x values and the variability of NO_x at the tropopause are in good agreement with the observations, while the mean values are too high due to the rare occurrences of very large values. Additionally, the 9-layer version of the GISS model has fairly coarse vertical resolution near the tropopause (~3-4 km), making the determination of which level best represents near-tropopause conditions ambiguous. Therefore, in Figure 7 we present NO_x values simulated at both the 200 and 320 mb levels compared with the NOXAR observations at the tropopause. Simulations performed to isolate individual contributions to the NO_x budget showed that transport is the dominant influence at the 200 mb level, while it is chemistry at the lower 320 mb level (Grewe et al., 2000). Except for the Northern spring, model values at 320 mb do quite a good job of matching the measured values. The values at 200 mb are quite a bit too large in spring and summer, though at least in spring, the vertical profile changes so sharply with altitude that the coarse model layers can be quite deceptive. These results imply that the chemistry scheme is in general doing a good job, while the dynamics near the tropopause need improvement (as seen in the ozone model/measurement comparison as well, though in those examples the stratospheric flux was too small, while here it seems too large, highlighting the complex temporal and geographical variability of stratosphere-troposphere exchange). The longitudinal variations seen by the aircraft instrument, with maxima over continental regions, are captured to a limited extent by the model. The model tends to give a more uniform distribution (especially at 200 mb), as does the European Center Hamburg (ECHAM) model, version 3 (Schumann et al., 2000) and version 4 (Grewe et al., 2000). Significant land-ocean contrasts are seen in most seasons at 320 mb in the GISS GCM, where chemistry largely governs the NO_x abundance. While the lack of NMHCs in the model could affect the results, it is not likely that it is responsible for the land-ocean contrast being somewhat reduced in the model as compared with observations. NMHCs lead to decreased NO_x concentrations in the upper troposphere over continental regions where convection occurs (Wang et al., 1998c), so would act to further reduce this contrast. The overall nitrogen oxide budget is shown in Table 3.

Overall, the model reproduces the large variation between summer and winter reasonably well, but misses the upper tropospheric maxima seen in observations during both equinox seasons. These maxima were also missed in the ECHAM4 model (Grewe et al., 2000). While there is some evidence that the 9-layer version of the GISS GCM has too little downward transport from 40-60N during both April and October (Rind et al., 1999), which could account for some of this discrepancy, it also seems to have too much downward transport during December, which is not seen in the present model/measurement comparison. More likely the two models both fail to calculate enough in situ production, due to too little transport of ozone precursors up from the boundary layer and/or too little production of NO_x from lightning at Northern Hemisphere middle latitudes.

A comparison of lightning flash frequencies observed by the Optical Transient Detector satellite instrument (Boccippio et al., 1998) and simulated in the GISS GCM is shown in Figure 8. The model parameterization generates lightning interactively with the GCM's convection scheme (Price and Rind, 1994; Price et al., 1997). The final lightning flash frequency in the model thus depends on both parameterizations, making it difficult to determine which is responsible for areas of disagreement (or even to be completely sure that correct areas do not result from a fortuitous cancellation of errors). These topics clearly deserve further study beyond the scope of this paper.

The model's flash frequency field captures many of the main features of the observed spatial distribution of lightning, including the large frequencies seen over tropical and subtropical continental regions. The global average flash rates in the model agree as well as can be expected with the observations, given that the data are from a single year. Some deficiencies are readily apparent, however. In the tropics, the model has a local maximum over the Indonesian archipelago during both seasons, while the observations favor Africa (though this could be a sampling bias). Similar results are seen in the observations for other years. The model parameterization also fails to reproduce observed lightning flash rates off the eastern edge of the continents (and over the oceans in general), especially over the Western Atlantic, and off of Southern Africa and Australia. The model underestimates continental lightning flash rates at Northern mid-latitudes over the continents as well, despite allowing overshooting of the top of a convective plume by one model layer in regions of very strong convection, such as at Northern middle latitudes. The model's underestimation can be clearly seen in the comparison of zonal mean lightning flash rates shown in Figure 9, which reveals distinct model underestimations from about 40N to 60N, in both the global and land-only averages, during June-August. A closer examination of the local flash frequencies shows that the model gives a flash rate up to an order of magnitude lower than observed over much of mid-latitude Eurasia. This underestimation suggest that underprediction of model ozone in some regions may be at least partially due to too little in situ production. This finding is in agreement with other model studies (e.g. Grewe et al., 2000) and with observational evidence (e.g. Graustein and Turekian, 1996; Jeker et al., 2000).

Despite these shortcomings, the global average summertime flash rate of 1.13 flashes km^{-2} per season in the model agrees quite well with the observed rate of 1.18 flashes km^{-2} per season for 1995 (other years are again similar). The production of nitrogen oxides from lightning involves further assumptions about the energy density per flash and the production amount per unit energy that are more difficult to validate. The total production is shown in Figure 10. Our value of 3.9 Tg/yr is close to the 'best' estimate of 5 Tg/yr, and well within the expected range of 2 to 20 Tg/yr (World Meteorological Organization, 1999).

3.4 Hydrogen Peroxide

A comparison of the model's hydrogen peroxide vertical profiles with aircraft observations (as shown in Wang et al., 1998b, Mickley et al., 1999, and Koch et al., 1999) is shown in Figure 11 (the model's hydroxyl distribution is shown in Figure 15, discussed in section 4). The model does a fairly good job of reproducing the observed profiles in the Northern subtropics based on the Japan Coast (~35N, 145E) and East China Sea regions (~25N, 130E). It is also able to capture the large abundances seen in the tropical South Atlantic (~10S, 20W) and Southern Africa (~15S, 25E) regions during the September biomass burning season. However, the large values seen during September over the Southern Brazilian coast (~30S, 50W) are not captured in the model, suggesting that emissions from biomass burning in South America may be too low (though the limited available data may not be representative of the longer term average). In the tropics, the model greatly overestimates low level (below about 600mb) amounts in the Western Equatorial Pacific (~5N, 150E) and Western Pacific (~10N, 155E) regions. At the same time, however, the model reproduces observations from the Pacific Exploratory Mission (PEM) - Tropics, in both the polluted Eastern Pacific and the remote central Pacific locals.

The GCM has roughly 50% more water vapor near the surface in the equatorial region than at 25N (East China Sea region), suggesting that the large hydrogen peroxide values at low altitudes near the equator may be due to chemical production. A comparison between the hydrogen peroxide budget derived here and that of Koch et al. (1999), given in Table 6, shows that while chemical production is indeed 20% larger, at the same time, the wet removal of H_2O_2 is 70% greater in this model, dry deposition at the surface is 38% less, and the tropospheric burden is also larger overall. Thus several factors lead to the large abundances at low levels in this model. The differences are especially large near the equator, where this chemistry model predicts much more hydrogen peroxide than was found in the Koch et al. (1999) simulations that used a prescribed OH distribution. At middle and high latitudes, differences between the two models are quite small. The results from this model are also fairly similar to those shown in Wang et al. (1998b) and Mickley et al. (1999), which also failed to simulate the very large abundances associated with South American biomass burning, though those models did not overestimate low altitude H_2O_2 over the western Pacific to as large an extent. Given the limited spatial and temporal coverage of the aircraft campaigns, it is difficult to clearly assess biases in the GCM. It seems, however, based on the Western Pacific comparisons, that this model likely has too much low level H_2O_2 in the equatorial region, especially in the Western Pacific. This may be related to outflow of polluted continental air from Asia.

4. Response to Pre-Industrial Conditions

In order to use this model for studies of the interaction between chemistry and climate, we must examine not only how well the model can simulate current conditions, but how it responds to changes. While little observational data is available from the pre-industrial period, many other models have looked at the changes from the pre-industrial to the present, making this a useful benchmark of model sensitivity. We therefore evaluate our model with respect to other models containing more detailed chemistry schemes by comparison of simulations using pre-industrial conditions. For the pre-industrial simulations, concentrations of long-lived greenhouse gases were reduced as follows: CO_2 from 365 to 280 ppmv, N_2O from 314 to 275 ppbv, CH_4 from 1.745 to 0.700 ppmv, and CFCs were reduced to zero. Emissions of ozone precursors were set to assumed pre-industrial values, so that NO_x and CO emissions from fossil fuel burning and aircraft were set to zero, while those from biomass burning were set to one-tenth their present day values, as in Mickley et al. (1999). NO_x emissions from soils were unchanged. Sulfate was set to natural background levels, assuming no anthropogenic component, as calculated in the GISS model (Koch et al., 1999). Sea-surface temperatures and sea ice coverage derived from a mixed-layer ocean run for pre-industrial conditions performed with an earlier version of this model (8 by 10 degree resolution) were used as the boundary conditions for the tropospheric chemistry simulation. Surface temperature changes between the present day simulations and the pre-industrial are shown in Figure 12. Values over the oceans reflect the warmer sea-surface temperatures and decreased sea-ice coverage of today's climate. Model results for pre-industrial conditions are taken from the last eight years of ten year runs, as two years were required for the model to equilibrate from present day conditions.

Tropospheric ozone has increased significantly since the beginning of the industrial age. Figure 13 shows zonal mean present day ozone mixing ratios, the change from pre-industrial to the present in units of mixing ratio, and the change from pre-industrial to the present in percent, relative to the pre-industrial amounts. Seasonal zonal mean ozone changes are shown in Part II. Table 7 presents the pre-industrial ozone budget (the tropospheric burden has been calculated using a 150 ppbv threshold to exclude stratospheric air, as for the present day). From Figure 13, it is clear that most of the increase has been in the Northern Hemisphere, where ozone abundances have increased by 20-40 ppbv in most of the troposphere northwards of 20N, in good agreement with the simulation of Stevenson et al. (1998). This represents more than a doubling of ozone in most of the lower troposphere, as seen in Mickley et al. (1999). At Northern mid-latitudes near the surface, values have increased by more than 125%. Ozone in the uppermost troposphere has increased by only 10-25%. As ozone at these altitudes is most important for climate change, the impact of ozone on climate has been much less than if the ground level increases persisted throughout the troposphere. We find an overall increase in the tropospheric ozone burden of 45%, in accord with the 25-57% range seen in other model studies (Table 7). This results primarily from decreased chemical production of ozone in the relatively unpolluted pre-industrial atmosphere. In fact, the net contribution to the ozone budget from photochemistry is negative during the pre-industrial period (-158 Tg yr^{-1} in our model, -30 to -323 Tg yr^{-1} in all studies), while it is positive in the present day in nearly all models.

Surface ozone is also much reduced in the pre-industrial period, shown in Figure 14, as compared with the present day (Figure 3). The global mean surface mixing ratio has increased by 57% from the pre-industrial to the present in January, and by 72% in July. For the annual average, the increase was 76% globally, with a 120% increase in the Northern Hemisphere, and a 31% increase in the Southern Hemisphere. Levy et al. (1997), using a chemical transport model, gave fairly similar numbers, though a somewhat smaller interhemispheric difference. They found a global increase of 66% in boundary layer ozone from pre-industrial to present, divided up into 73% in the Northern Hemisphere extratropics, 71% in the tropics, and 43% in the Southern Hemisphere extratropics. Very large differences from pre-industrial to present in our model are seen over the continents year round, but also over the Northern Hemisphere oceans all the way to the equator during January. Another region of note is the northern portions of the Northern Hemisphere continents during July, which had ozone levels similar to the remote ocean during the pre-industrial period, but are fairly polluted during the present.

Our values are qualitatively similar to those shown in Mickley et al. (1999). Both have patches of ozone below 10 ppbv over the tropical oceans, and fairly large areas with between 20 and 30 ppbv ozone over the Southern Ocean during July, but not during January. Our model tends to have somewhat larger values over the Northern Hemisphere continents during July (20-40 ppbv versus 15-30 ppbv), but not during January. The GISS values are also similar to those presented by Lelieveld and Dentener (2000), who also found ozone levels below 10 ppbv over the tropical oceans, and between 20 and 30 ppbv over the Southern Ocean. Their May-August surface ozone (they do not show January), with values from 20 to 40 ppbv, are closer to those seen in the GISS model than those in Mickley et al. (1999). The Lelieveld and Dentener model found much lower pre-industrial surface ozone levels over Antarctica than the other two, however (as for the present day, see Table 4). Roelofs et al. (1997) show modeled pre-industrial surface ozone levels at Payerne (47N) and Mace Head (53N), which are both in the range of 10-20 ppbv during July, closer to the smaller Mickley et al (1999) values than the amounts seen in Lelieveld and Dentener (2000) or in this work. The variations are perhaps indicative of the uncertainty surrounding pre-industrial surface ozone levels. As discussed in Wang and Jacob (1998), most models find surface ozone values that are slightly larger over Europe and South America as compared with what little data is available (Marenco et al., 1994).

The oxidation capacity of the troposphere may have also changed since pre-industrial times. This could greatly impact the chemical lifetimes of many trace gases which are radiatively or chemically important, such as chlorofluorocarbons, carbon monoxide, methane, and other hydrocarbons. Our simulation shows a net decrease in the tropospheric oxidation capacity from the pre-industrial to the present through most of the tropics and in the Southern Hemisphere, with an increase in most of the Northern Hemisphere extra-tropics (Figure 15 - Seasonal changes are shown in Part II). The modeled global mean OH abundance for the present day was 9.76×10^5 molecules cm^{-3}, while the pre-industrial value was 10.37×10^5 molecules cm^{-3}. Globally, this represents a net decrease of 5.9% since the pre-industrial period. Note that the present day value agrees quite well with the $9.7 \pm 0.6 \times 10^5$ molecules cm^{-3} derived from observations of the lifetime of the solvent methyl chloroform (Prinn et al., 1995). A range of results has been found in other models. Brasseur et al.

(1998) found a decrease of 17% in global OH, Mickley et al. (1999) found a decrease of 16%, Wang and Jacob (1998) found a 9% decrease, and Berntsen et al. (1997) found a 6% increase. Several lower-dimensional models also found decreases in global OH from the pre-industrial to the present (Thompson, 1992). Assumed conditions during the pre-industrial era vary widely from model to model, as emissions such as those from biomass burning are not well known, which may account for some of the large spread in the model results. We also note that our runs included altering not only emissions of ozone precursors to pre-industrial levels, but also lowering sulfate aerosol, greenhouse gases, and ocean temperatures and sea ice coverage. These modifications are not commonly included, but all affect OH abundances. Increased temperatures and humidity in the present day both enhance OH, while the greater amount of sulfate reduces NO_x and hence OH. The net effect is to reduce the pre-industrial to present day decrease in the oxidation capacity of the troposphere by about half, as discussed more fully in Part II, likely accounting for our falling at the low end of the range seen in other models.

As removal of methane from the atmosphere takes place primarily via oxidation by OH, changes in OH abundances have a large impact on the lifetime of methane. Since methane has contributed the second largest component to the positive radiative forcing since the pre-industrial period, after carbon dioxide (Hansen et al., 1998), it is important to assess how it may have been affected by changing oxidation. Most models find that reduced oxidation capacity has lead to a slower removal of methane emissions from the atmosphere. Brasseur et al. (1998) and Stevenson et al. (1998) found increases in the methane lifetime of 1.5 and 1.3 years, respectively. Our simulations also show an increase in methane's lifetime since pre-industrial times, but of only 0.4 years, as our oxidation change is less. Note that for the present day, we find a total methane oxidation rate of 492 Tg yr^{-1}, in good agreement with the recommended value of 490 Tg yr^{-1} given in the International Panel on Climate Change (1996).

Changes in ozone have resulted primarily from changes in emission of ozone precursors, rather than climate change (see Part II). This is because the abundance of precursors has increased by such a large amount. At Northern Hemisphere mid-latitudes, where the majority of industrialized countries lie, increases in nitrogen oxide abundances have exceeded 1000%, and in carbon monoxide they have exceeded 800%, as shown in Figure 16. These modeled increases are similar in location and magnitude to those shown in Mickley et al. (1999). These changes have dominated the lesser influence of changing temperature and humidity resulting from the increase of greenhouse gases in the atmosphere. We note that the NO_x changes include an increase in emissions from lightning of 0.3 Tg N (9% of the pre-industrial value), which is attributable to climate change rather than anthropogenic emissions.

5. Influence of chemistry-climate coupling

The model has been set up to run with the radiative transfer calculation either responding to the calculated, chemical ozone values (radiatively coupled mode) or using the standard ozone climatology (radiatively uncoupled mode). Comparing the results of the two allows us to discern the influence of the coupling between the ozone chemistry and the radiation on the chemistry itself.

The impact is small for the present day simulation, as climatological ozone values are quite similar to those calculated for current conditions. We find differences in zonal mean ozone of only about ±2 ppbv between the coupled and uncoupled modes. The only statistically significant changes are in the tropical upper troposphere, where the model's ozone values are 1-2 ppbv greater in the radiatively coupled mode. That these differences are quite small is no surprise however, since the ozone climatology has been created from observations taken during the 1980s.

Of greater interest is how the coupling affects the pre-industrial simulation. Figure 17 shows the difference between the coupled and uncoupled modes for zonal mean ozone and hydroxyl during the pre-industrial era. Since the climatological values are similar to the present day calculated values, this difference is also almost identical to the influence of chemistry-radiation coupling on the pre-industrial to present day changes. Since the pre-industrial period, ozone values have increased by 20-40 ppbv in much of the Northern Hemisphere, and 1-10 ppbv in much of the Southern Hemisphere, according to the model simulations (as shown in Figure 13). Changing from uncoupled to coupled mode had a minimal effect on the Northern Hemisphere, altering the ozone change by 2% or less (generally reducing the pre-industrial-to-present change), since the huge increase in precursor emissions dominated the overall ozone change. In the Southern Hemisphere, the chemistry-radiation coupling played a relatively more important role, accounting for about 3-7% of the increase there. This still represents a small amount of ozone, given that the total increase was less than 10 ppbv. Globally, the chemical-radiative coupling creates only about a tenth of one percent more ozone. We conclude that to a very good approximation, the use of on-line interactively calculated ozone fields is not necessary to properly simulate the ozone distribution for either the current climate or pre-industrial conditions, though this may not be true for future conditions.

The results for hydroxyl are more interesting (Figure 17). While changes are small, nearly all the changes in OH from including the chemical-radiative coupling are positive. The decrease in OH from the pre-industrial to the present is therefore enhanced going from -5.3% in the uncoupled mode to -5.9% in the coupled mode. In our pre-industrial simulations, the change in tropospheric oxidation capacity is also influenced by reduced sulfate aerosol, greenhouse gases, ocean temperatures and sea ice coverage (see Part II for further details). As noted in Section 4, these factors are commonly neglected, but have significant effects. We conclude that while the range of oxidation capacity changes seen in various models is quite large, they may all suffer from systematic biases, in both directions depending on the factors overlooked, in their estimation of the oxidation capacity change over time.

6. Radiative Forcing

The global mean annual average radiative forcing at the top of the atmosphere due to the tropospheric ozone increase since the pre-industrial period is 0.32 W/m^2 in these simulations. The forcing is predominantly in the Northern Hemisphere, where it is 0.50 W/m^2, compared with 0.14 W/m^2 in the Southern Hemisphere. The spatial distribution (Figure 18) shows the largest values over the continents at latitudes from around 15 to 45 N, and at high Northern latitudes. This pattern is in general agreement with available results from previous simulations (Berntsen et al., 1997; Stevenson et al., 1998; Haywood et al., 1998).

Radiative forcing was calculated by calling the radiation code twice: once with the climatological ozone values and once with the values calculated by the chemistry routines. This was done for both the pre-industrial and the present day simulations, so that the final values are: (present day flux with calculated ozone minus flux with climatological ozone) minus (pre-industrial flux with calculated ozone minus flux with climatological ozone). Though it seems that the climatological ozone term should cancel out, the difference must be taken in each time period to remove the impact of meteorological differences between the two runs. The final forcing thus results solely from the difference between the ozone calculated by the model's chemistry in each time period. Furthermore, the ozone calculation includes the response to climate change, imposed by increasing greenhouse gas concentrations (affecting temperatures and meteorology) and altered ocean/sea ice boundary conditions. Radiative fluxes are calculated every five hours in the GCM. The calculation with the ozone climatology was used to drive the meteorology, which was therefore identical in the two simulations outside of internal variability.

As a test, we also ran the model in the coupled mode, but this made little difference, yielding a forcing of 0.01 W/m^2 larger than that in the uncoupled mode, with most of the increase in the Arctic. (Note that the coupling was incomplete, as the radiative changes were only allowed to affect the atmosphere and land temperatures, and not the sea-surface temperatures or sea-ice, which may have reduced their impact.) A difficulty in interpreting this result is that the forcing calculation in the coupled mode is inherently an adjusted forcing, not an instantaneous one, since in a fully interactive model, stratospheric temperatures relax to equilibrium following tropospheric ozone perturbations. Adjusted forcing is approximately 0.02 W/m^2 less than the instantaneous forcing for the same perturbation in other models (e.g Berntsen et al., 1997; Haywood et al., 1998), however. The change from instantaneous to adjusted forcing, while more realistic since the atmosphere is allowed to respond to forcing, may therefore have compensated for this portion of the total change due to the coupling of the calculated ozone to the radiation, which may in fact have increased the radiative forcing by roughly 0.03 W/m^2, about 10%. That the overall influence of coupling would be positive is consistent with chemical-radiative coupling leading to an overall increase in the ozone burden. Furthermore, the increase is largest in the upper troposphere, where ozone impacts radiative forcing most strongly, suggesting that the 10% increase is probably the more appropriate one.

Seasonal radiative forcing values are largest in Norther Hemisphere spring and summer (Figure 19). Especially large values, greater than 1.0 W/m^2, are seen during those times over the United States, the Middle East, North Africa, and the Mediterranean, and over large portions of Central Asia. The highest values, larger than 1.5 W/m^2, occur over Southern California, northwestern India and Pakistan during spring, Central Asia east of the Caspian Sea, and the Arctic. These distributions are overall quite similar to those found using more detailed chemistry in the GISS GCM (Mickley et al., 1999) at most times over most of the globe. The summer maxima described above match extremely well with the more complex model. Primary exceptions are the Southern Atlantic during September-November, when the forcing is larger in the Mickley et al model, and the Arctic during March-May, when the forcing is much smaller in the other model. The former difference is likely related to a reduced influence of biomass burning in this region due to an NO_x biomass burning source more than 50% smaller than that used by Mickley et al. (1999) (the actual value is quite uncertain), and perhaps also to the lack of burning emissions of higher hydrocarbons. A clue to the Arctic differences can be gained by examining the shortwave and longwave components separately. The December-February (DJF) and July-August (JJA) values are shown in Figure 20. The very large forcing values seen in this model over the Arctic result predominantly from changes in the shortwave. This is expected, as the high ice albedo over Greenland and the Arctic is very effective at reflecting sunlight, which can then be absorbed by the additional ozone. While shortwave forcing also maximizes over the Arctic during JJA in the more complex model of Mickley et al., the forcing is not quite as large as that shown here. The same bias likely affects the March-May results even more strongly. Figure 1 showed that the simulations overestimated the amount of ozone at Resolute (75 N) in the lower troposphere from around 500 - 800 mb (carbon monoxide values were also overestimated in the Arctic, as shown in Figure 4). Since even small amounts of ozone can have a large effect on the forcing in the shortwave, this bias is probably responsible for most of the large forcing values in the Arctic during sunlit periods. However, the model underestimated ozone in the lower stratosphere at 200 mb, which might have been expected to contribute even more strongly to reducing the radiative forcing. Figure 1 also showed that the model did a fairly good job of reproducing ozone values outside the Arctic, in accord with it's ability to reproduce the more complex model's radiative forcing values across most of the rest of the globe quite well.

Our calculated global annual average radiative forcing from anthropogenic ozone of 0.32 W/m^2 lies within the range of 0.28 - 0.55 W/m^2 found in other three-dimensional global models (Hauglustaine et al., 1994; Roelofs et al., 1997; van Dorland et al., 1997; Berntsen et al., 1997; Stevenson et al., 1998; Haywood et al., 1998; Brasseur et al., 1998; Kiehl et al., 1999; Mickley et al., 1999; Lelieveld and Dentener, 2000). It is similar to, though somewhat less than, the 0.44 W/m^2 found in the Mickley et al. (1999) model. The values are especially similar in the Northern Hemisphere (0.50 W/m^2 versus 0.53 W/m^2), while the discrepancy arises primarily from the lower value seen in our model in the Southern Hemisphere (0.14 W/m^2 versus 0.34 W/m^2). This is partially due to the much larger NO_x biomass burning source used in the Mickley et al. (1999) study. Additionally, Mickley et al. reduced the emissions of NO_x from soils in the pre-industrial, and we did not. These differences in NO_x take on a greater importance in the less polluted Southern Hemisphere. Furthermore, the small amount of radiative forcing seen in the Southern Hemisphere is strongly influenced by the retreat of sea ice around Antarctica from the pre-industrial to the present (see Figure 12). As greenhouse gases buildup in the atmosphere, the resulting global warming affects surface temperatures globally. Where sea ice is present, however, there is an additional ice-albedo feedback on warming, since warmer temperatures melt ice, reducing the surface albedo, hence further warming the surface (this feedback is not include in these chemistry runs with prescribed ocean/ice conditions, but was included in the original simulations that derived the conditions used here). This is seen most strongly at the Antarctic sea ice margin in the model, where small temperature changes can have a large effect as the temperatures are near the threshold for formation and maintenance of sea ice. The decreased albedo resulting from the sea-ice retreat compensates for a large fraction of the increase of ozone in the Southern Hemisphere. While the greater ozone abundance in the present day increases the radiative forcing, the reduced shortwave reflectivity of the surface reduces the forcing per unit ozone. One need only look at the very large shortwave forcing values found over the Arctic (Figure 20) to see the importance of the high albedo (discussed above). While the shortwave forcing during Northern Hemisphere summer is greater than 1.5 W/m^2 over a large portion of the Arctic, it is only about 0.1 W/m^2 over a similar sized area of the Antarctic during the Southern summer (Figure 20). This is a far greater relative difference than that seen in ozone, which increased by about 5 ppbv over the Antarctic sea ice margin, and by about 30 ppbv over the Arctic sea ice margin.

Overall, the radiative forcing in the Southern Hemisphere is smaller in this model due to several factors. The primary influences are the different biomass burning and soil sources of NOx, a greater amount of sea-ice around Antarctic in the pre-industrial era, and the smaller overall change in total ozone. Our increase in the ozone burden was 82 Tg, as compared with 130 Tg in Mickley et al. (1999).

7. Discussion/Conclusions

We have developed a simplified, fast tropospheric chemistry model which runs interactively within the GISS climate model. The model is largely able to reproduce observed ozone vertical profiles and annual cycles, despite the relatively simple chemistry scheme used. The lack of non-methane hydrocarbon chemistry in the model does not seem to greatly affect the quality of the simulated ozone field, in accord with other modeling studies (e. g. Wang et al., 1998c). The model also calculates radiative forcing values due to anthropogenic ozone that are quite similar to those seen in other, more complex models. This is not surprising, given that the model does a good job with the ozone distribution itself. However, though most of the chemical transport models or coupled chemistry-climate GCMs also reproduce these observations, there remain significant differences in the ozone budgets of the various models. The large range of ozone budget terms that seem able to yield ozone values in agreement with measurements indicates that large uncertainties persist in understanding the relative importance of the various factors governing tropospheric ozone abundances.

The model has been compared extensively throughout this paper with the results from a more detailed chemistry module which has also been used within the GISS GCM (Mickley et al., 1999). Though the models use the same basic GCM, so that the dynamics and meteorology are calculated identically, there are several differences besides the chemical schemes. This model uses a somewhat newer version of the GCM, with several improvements to the convection scheme amongst other changes. In these simulations, we also allowed the model to calculate transport from the stratosphere to the troposphere, while this was prescribed in the Mickley et al. (1999) work. This study also assumed a smaller present day biomass burning source of nitrogen oxides, and kept NO_x from soils constant over time. For the pre-industrial period, we included altered sulfate and ocean surface conditions, which were kept at present day values in the simulation of Mickley et al. (1999). Nevertheless, for quantities which are lacking in observations, comparison with the more detailed model has provided an important test of the validity of using a simplified chemistry scheme for climate studies.

In general, the simplified chemistry model performs quite well. Noticeable differences include present day ozone over the South Atlantic during fall, where the Mickley et al. model has larger ozone amounts, likely as a result of greater emissions from biomass burning. Given that both models have difficulties in matching observations of hydrogen peroxide or nitrogen species in this area, it is not obvious which is performing better. Another difference is reduced Southern Hemisphere radiative forcing from anthropogenic ozone, which we attribute largely to the Antarctic sea ice changes imposed on the model. It also appears that our model had greater difficulty with stratosphere-troposphere exchange. This is especially evident in the Arctic, where the current work overestimates ozone abundances. We hope to improve the representation of the exchange process in future versions, tests of which have already shown considerable advances. Overall, the contribution of chemistry to the ozone budget was quite similar in the two models (370 Tg/yr in Mickley et al versus 389 Tg/yr in this work, out of a range of -810 Tg/yr to +550 Tg/yr in other models), and the overall ozone distributions were also fairly similar.

The calculated radiative forcing is most important for climate studies. The model calculates a radiative forcing from tropospheric ozone between the pre-industrial and the present of 0.32 W/m^2. We find that coupling the calculated ozone to the GCM's radiation, and hence, to the meteorology, has a fairly small impact. It increases the radiative forcing by about 3%, though since this is an adjusted forcing, which is typically about 6% less than an instantaneous forcing (the 0.32 W/m^2 value found in the uncoupled mode), coupling the ozone to the radiation has likely increased the radiative forcing by approximately 10% (0.03 W/m^2). In general, the distribution and magnitude of the radiative forcing due to pre-industrial to present day ozone increases matched quite well with the more detailed model of Mickley et al. (1999), and is similar to other models as well. Therefore, we believe that this coupled chemistry-climate model can be used for realistic climate studies. Since it uses simplified chemistry, and therefore runs quite rapidly, it is ideally suited to study issues such as the relative importance of individual aspects of chemistry-climate interactions over time (e.g. changes in greenhouse gases, ocean temperatures and sea ice coverage, individual emission sources, lightning etc.), which require many simulations.

Acknowledgements

We thank Loretta Mickley, Dorothy Koch, Daniel Jacob, Jennifer Logan, and William Koshak for providing advice and data, and Michael Prather and Oliver Wild for providing the photolysis code. MAPS data were obtained from the Langley DAAC. The Global Hydrology Resource Center at the Global Hydrology & Climate Center supplied the archived OTD data. Thanks to Mr. John Hall (Computer Sciences Corporation, Huntsville, AL) for generating the OTD seasonal data files, and to Rick Healy for providing the pre-industrial ocean boundary conditions.

Table 1. Chemical reactions included in the model.

	Bimolecular Reaction	A-Factor	Activation Temperature
1	OH + HO2 --> H2O + O2	4.80E-11	-250.
2	OH + O3 --> HO2 + O2	1.60E-12	940.
3	OH + OH --> H2O + O	4.20E-12	240.
4	HO2 + O3 --> OH + O2	1.10E-14	500.
5	O3 + NO --> NO2 + O2	2.00E-12	1400.
6	HO2 + NO --> OH + NO2	3.50E-12	-250.
7	NO2 + O3 --> NO3 + O2	1.20E-13	2450.
8	O(1D) + O2 --> O + O2	3.20E-11	-70.
9	O(1D) + M --> O + M	1.30E-11	-110.
10	O(1D) + H2O --> OH + OH	2.20E-10	0.
11	O(1D) + CH4 --> OH + CH3O2	1.50E-10	0.
12	CH4 + OH --> H2O + CH3O2	2.45E-12	1775.
13	CO + OH --> HO2 + CO2	1.50E-13	0.
14	OH + H2O2 --> H2O + HO2	2.90E-12	160.
15	HO2 + HO2 --> H2O2 + O2	2.30E-13	-600.
16	OH + HNO3 --> H2O + NO3	7.20E-15	-785.
17	NO3 + NO --> NO2 + NO2	1.50E-11	-170.
18	OH + HO2NO2 --> H2O + NO2	1.30E-12	-380.
19	H2 + OH --> HO2 + H2O	5.50E-12	2000.
20	CH3O2 + NO + HO2 --> HCHO + NO2	3.00E-12	-280.
21	HCHO + OH + H2O --> HO2 + CO	1.00E-11	0.
22	CH3O2 + HO2 --> CH3OOH + O2	3.80E-13	-800.
23	CH3OOH + OH --> CH3O2 + H2O	3.80E-12	-200.
24	NO2 + NO3 --> NO + NO2 + O2	4.50E-14	1260.
25	NO3 + NO3 --> NO2 + NO2 + O2	8.50E-13	2450.
26	OH + HONO --> H2O + NO2	1.80E-11	390.
27	CH3O2 + CH3O2 --> HCHO + HCHO	2.25E-13	-190.
28	NO3 + HCHO --> HNO3 + CO + HO2	5.80E-16	1900.

	Monomolecular Break-up reaction (rates for equilibrium constants)	A-Factor	Temperature Dependence
29	HO2NO2 + M --> HO2 + NO2	2.10E-27	10900.
30	N2O5 + M --> NO3 + NO2	2.70E-27	11000.

	Termolecular reactions	k_o	n	k_∞	m
31	O + O2 + M --> O3 + M	6.00E-34	2.3	0.00E-00	0.0
32	NO + O + M --> NO2 + M	9.00E-32	1.5	3.00E-11	0.0
33	OH + OH + M --> H2O2 + M	6.20E-31	1.0	2.60E-11	0.0
34	OH + NO2 + M --> HNO3 + M	2.50E-30	4.4	1.60E-11	1.7
35	HO2 + NO2 + M --> HO2NO2 + M	1.80E-31	3.2	4.70E-12	1.4
36	NO3 + NO2 + M --> N2O5 + M	2.20E-30	3.9	1.50E-12	0.7
37	OH + NO + M --> HONO + M	7.00E-31	2.6	3.60E-11	0.1

	Heterogeneous reactions
38	N2O5 + H2O --> 2 HNO3

Reaction rates for bimolecular reactions are given by Aexp((-E/R)(1/T), where A is the Arrhenius A-factor, E/R is the activation temperature of the reaction, and T is the temperature. For monomolecular reactions, the equilirbium constant is given by Aexp(B/T), where A is again the A-factor, and B is the temperature dependence of the reaction. For termolecular reactions, rates are calculated as a function of the high and low pressure reactions rates, given by $k_\infty(T/300)^{-m}$ and $k_0(T/300)^{-n}$, respectively, where T is temperature. In all the above reactions, 'M' is any body that can serve to carry away excess energy. Reaction 9 is multiplied by 0.72 to include only quenching reactions on molecular nitrogen, since reaction 8 accounts for those on oxygen molecules. Reactions 11 and 12 assume an instantaneous reaction of the methyl radical with oxygen to form CH3O2. Reactions 13, 15 and 16 include additional dependencies on pressure, pressure and water vapor, and pressure and temperature, respectively. Reaction 27 is multiplied by 0.9 to account for the yield of these products, and includes a 33% yield of two HO2 molecules. Reaction 28 is approximate.

Table 2. Photolysis reactions included in the model.

1	NO2 --> NO + O
2	O3 --> O(1D) + O2
3	O3 --> O + O2
4	H2O2 --> OH + OH
5	NO3 --> NO + O2
6	NO3 --> NO2 + O
7	N2O5 --> NO3 + NO2
8	HONO --> OH + NO
9	HNO3 --> OH + NO2
10	HO2NO2 --> HO2 + NO2
11	HO2NO2 --> OH + NO3
12	HCHO --> CO + H2
13	HCHO --> CO + HO2
14	CH3OOH --> HCHO + HO2

Table 3. NOx budget (Tg N/yr - Annual mean)

Fossil Fuels	22.6
Soils	5.9
Biomass Burning	5.3
Lightning	3.9
Aircraft	0.6
Stratosphere	0.2
Chemistry	-33.2
Dry Deposition	-5.3

Table 4. Surface Ozone (ppbv)

	January West Africa maximum	January, North Atlantic	July, Eastern United States	July, South-West Africa Maximum	July, Coastal Antarctica, 30-50 E
Roelofs and Lelieveld (1995)	30-40	20-25	30-50	40-50	10-15
Müller and Brasseur (1995)	30-35	35-45	40-50	28-35	12-18
Collins et al. (1997)	60-80	20-40	120-140	60-100	0-20
Berntsen and Isaksen (1997)	35-40	25-35	40-55	25-35	10-20
Wang et al. (1998b)	60-70	30-40	40-70	50-70	20-30
Lawrence et al. (1999)	20-30	20-30	30-40	30-50	10-20
Mickley et al. (1999)	70+	30-40	40-60	50-70	20-30
Lelieveld and Dentener (2000)	--	--	60-70	30-50	15-20
This work	60 -65	30-50	50-80	30-60	20-30
Observations		Atlantic Islands 30-40	Wallops Island (38N, 76W) 59 ± 18	Brazzaville (4S, 14E) 33 ± 6	Syowa (69 S, 39E) 29 ± 5

Values are January and July monthly means, except in the following cases, where we used the closest available data: Roelofs and Lelieveld (1995) are December-February and June-August averages, Müller and Brasseur (1995) are for day 360 in December and day 180 in June, Collins et al. (1997) are for February and August, and Lelieveld and Dentener (2000) are for May-August. North Atlantic island observations are the January monthly mean range based on 4 years of data from Sable Island (44N, 60W) and one year of data from Azores (39N, 28W) as given by Parrish et al (1998). Ozonesonde data for Wallops Island, Brazzaville, and Syowa are from Logan (1999).

Table 5. Ozone Budget

	Chemistry	Dry Deposition	Stratosphere	Burden
Roelofs and Lelieveld (1995)	+170	-740	+575	236
Müller and Brasseur (1995)	+550	-1100	+550	--
Lawrence (1996)	+30	-641	+594	--
Berntsen and Isaksen (1997)	+295	-1178	+846	--
Levy et al. (1997)	+128	-825	+696	298
Roelofs et al. (1997)	+75	-534	+459	271
Houweling et al. (1998)	-86	-681	+768	311
Wang et al. (1998b)	+420	-820	+400	310
Hauglustaine et al. (1998)	+507	-1237	+391	364
Crutzen et al. (1999)	-810	-620	+1440	--
Lawrence et al. (1999)	-478	-621	+1103	--
Mickley et al. (1999)	+370	-760	+390	360
Stevenson et al. (2000)	+430	-862	+432	316
Lelieveld and Dentener (2000)	+140	-705	+565	347
This work	+389	-1140	+750	262

Values are given in Tg/yr for sources and sinks, and Tg for the total burden. All values are annual means. Note that Mickley et al. (1999), Roelofs et al. (1997), Roelofs and Lelieveld (1995), and this study used chemistry included within general circulation models, while the other studies used off-line chemical transport models.

Table 6. H2O2 budget

	This work	Koch et al (1999)
Dry Chemistry	+360	+300
Dry Deposition	-88	-141
Wet Deposition	-236	-125
Wet Chemistry	-34	-34
Loss to Stratosphere	-2	--
Burden	6.4	4.2

Values are given in Tg/yr for sources and sinks, and Tg for the total burden. All values are annual means.

Table 7. Pre-Industrial Ozone Budget

	Chemistry (Tg yr^{-1})	Dry Deposition (Tg yr^{-1})	Stratosphere (Tg yr^{-1})	Burden (Tg)	Burden Increase to Present (Tg)
Levy et al (1997)	-234	-459	+696	215	83 (39%)
Roelofs et al (1997)	-323	-296	+622	190	81 (43%)
Mickley et al (1999)	-30	-360	+390	230	130 (57%)
Lelieveld and Dentener (2000)	-162	-444	+606	278	69 (25%)
This work	-158	-625	+782	180	82 (45%)

Values in parentheses in the last column show percentage increases in the tropospheric ozone burden from pre-industrial to the present, relative to the pre-industrial burden. All values are annual means.

Figure Captions

Figure 1. Comparison of observed and simulated annual cycles of ozone at the indicated altitudes and locations. Open triangles and dotted lines indicate ozonesonde measured mean values and standard deviations, respectively. Solid circles and dashed lines show modeled mean values and standard deviations. All values are mixing ratios in ppbv. The coordinates are, from left to right, Resolute (75 N, 95 W), Hohenpeissenberg (48 N, 11 E), Hilo (20 N, 155 W), Natal (6 S, 35 W), Lauder (45 S, 170 E), and Syowa (69 S, 39 E). Data records at these locations are from 5 to 15 years long, and include between 217 and 1615 individual measurements (Logan, 1999).

Figure 2. Comparison of observed and simulated ozone profiles at the given locations in January (top row) and July (bottom row). Open triangles and dotted lines indicate ozonesonde measured mean values and standard deviations, respectively. Open circles and dashed lines show modeled mean values and standard deviations for the standard simulation (S), while filled circles and dashed lines are from the simulation with reduced ozone in the stratosphere (R). The coordinates of the locations are: Sapporo (43 N, 141 E), Wallops Island (38 N, 76 W), Natal (6 S. 35 W), and Pretoria (26 S, 28 E). Data records at these locations are from 3 to 16 years long, and include between 136 and 388 individual measurements (Logan, 1999).

Figure 3. Modeled ozone values (ppbv) in the lowest model layer for the present day. The top panel shows January near-surface values, while the bottom shows July. Numbers in the upper right of each panel give area weighted global mean values for comparison with pre-industrial values (Figure 14).

Figure 4. Comparison of observed and simulated carbon monoxide near the surface. Open triangles and dotted lines indicate measured mean values and standard deviations, respectively. Solid circles and dashed lines show modeled mean values and standard deviations at the 959 mb level.

Figure 5. Observed and modeled global carbon monoxide (column mean mixing ratio in ppbv). Measurements were taken by the Measurement of Air Pollution from Satellites (MAPS) instrument. The top row shows values for April (observations from 1994, model values from the 'present day' simulation), while the middle row shows similar plots for October. The bottom right panel presents measurements taken ten years earlier, during October 1984. Model output has been weighted similarly to MAPS (see text for details), so that the two values are comparable. All plots use the same color scale.

Figure 6. Seasonal mean values of NOx (NO+NO2+NO3) volume mixing ratios (pptv) in the middle and upper troposphere. Profiles measured by the NOXAR aircraft, which flew almost entirely between 40 and 60N, and 90W to 120E (heavy line) (Grewe et al., 2000) and simulated by the GCM for the same locations (dotted line with one standard deviation uncertainties) are shown. The density of aircraft measurements is shown on the right side of each plot.

Figure 7. Measured NOx in the tropopause region (± 25 hPa relative to the local tropopause) from NOXAR as in Figure 6. The nearest GISS model levels at 200 hPa and 320 hPa are shown as thin and dashed lines, respectively. The inter-annual standard deviation is also included for the models (bars). The number of NOXAR measurements per 3.75 degrees is shown along the top of each plot.

Figure 8. Lightning flash frequency (flashes km^{-2} per season). The top row shows June-August data, while the bottom row shows December-February data. The left column shows values observed from June 1995 to February 1996 (other years are fairly similar) by the Optical Transient Detector instrument (Boccippio et al., 1998), while the right column shows the nine year average from the model simulation.

Figure 9. Zonal mean lightning flash frequency (flashes km^{-2} per season) during June-August (top) and December-February (bottom) calculated from the data and simulations shown in Figure 8.

Figure 10. Seasonal cycle of nitrogen oxide production from lightning in the present day simulation.

The result is a nine-year average.

Figure 11. Comparison of observed and simulated hydrogen peroxide profiles at the indicated locations. Open triangles and dotted lines indicate aircraft measured mean values and standard deviations, respectively. Solid circles and dashed lines show modeled mean values and standard deviations. The coordinates at the approximate center of the regions are shown. See Wang et al. (1998b) and Koch et al. (1999) for exact areas of aircraft campaigns.

Figure 12: Annual average surface temperature change from the pre-industrial to the present calculated in the model. Ocean changes primarily reflect the sea-surface temperature and sea-ice coverage changes which are prescribed based on an earlier run of the GISS GCM. The global mean temperature increase is 1.76 K. The contour interval is one degree K. Values below 1 are white, those between 1 and 3 are shaded light grey, and those above 3 are darker grey.

Figure 13: Zonal mean ozone and ozone changes in the model. The left panel shows zonal mean present day ozone mixing ratios. The center panel shows the change from pre-industrial to the present in units of mixing ratio (ppbv). The right panel shows the same change from pre-industrial to the present, but in percent relative to the pre-industrial amounts.

Figure 14: Near surface modeled ozone values (ppbv) in the pre-industrial period. The top panel shows January values in the lowest model layer, while the bottom shows July. Large values over Greenland, the Himalayas, and Antarctica result from the model's use of terrain following coordinates, so that the lowest model level is at a much higher altitude in these regions where the orography is high. Numbers in the upper right of each panel give area weighted global mean values for comparison with present day values (Figure 3).

Figure 15: Zonal mean hydroxyl in the present day simulation (left side), and the zonal mean hydroxyl change from the pre-industrial to the present (right side). Both panels give values in units of 10^5 molecules cm^{-3}.

Figure 16: Modeled zonal mean change in percent for nitrogen oxides (left) and carbon monoxide (right) from the pre-industrial to the present.

Figure 17: The impact of coupling the calculated ozone to the GCM's radiation and meteorology. Zonal mean differences of the coupled minus the uncoupled modes for ozone (left - in tenths of ppbv) and hydroxyl (right - in units of 10^4 molecules cm^{-3}) for the pre-industrial period.

Figure 18: Global mean annual average radiative forcing at the top of the atmosphere due to the tropospheric ozone increase since the pre-industrial period (W/m^2). The global mean value, 0.32 W/m^2 is shown in the upper right. Results are shown from simulations without ozone feedback onto the GCM's meteorology, though inclusion of this interaction has a small effect on the results (see text).

Figure 19: Seasonally averaged global mean radiative forcing at the top of the atmosphere due to the tropospheric ozone increase since the pre-industrial period (W/m^2), from the same runs as in Figure 18. Global mean values are shown in the upper right corner of each plot.

Figure 20: Longwave (top) and shortwave (bottom) radiative forcing at the top of the atmosphere due to the tropospheric ozone increase since the pre-industrial period (W/m^2), from the same runs as in Figure 18. Seasonal values are given for December-February (left) and July-August (right), and global mean values are shown in the upper right corner of each plot.

References

Baughcum, S. L., T. G. Tritz, S. C. Henderson, and D. C. Pickett, Scheduled Civil Aircraft Emission Inventories for 1992: Database Development and Analysis, NASA CR-4700, 1996.

Benkovitz, C. M., M. T. Scholtz, J. Pacyna, L. Tarrason, J. Dignon, E. C. Voldner, P. A. Spiro, J. A. Logan, and T. E. Graedel, Global gridded inventories of anthropogenic emissions of sulfur and nitrogen, *J. Geophys. Res.*, 101, 29,239-29,253, 1996.

Berntsen, T. K., I. S. Isaksen, G. Myhre, J. S. Fuglestvedt, R. Stordal, T. A. Larsen, R. S. Freckleton, and K. P. Shine, Effects of anthropogenic emissions on tropospheric ozone and its radiative forcing, *J. Geophys. Res.*, 102, 28,101-28,126, 1997.

Berntsen, T. K., and I. S. Isaksen, A global three-dimensional chemical transport model for the troposphere: 1, Model description and CO and ozone results, *J. Geophys. Res.*, 102, 21,239-21,280, 1997.

Boccippio, D. J., K. Driscoll, W. Koshak, R. Blakeslee, W. Boeck, D. Mach, H. J. Christian, and S. J. Goodman, Cross-sensor validation of the Optical Transient Detector (OTD), *J. Atmos. Sol. Terr. Phys.*, 60, 701-712, 1998.

Brasseur, G. P, J. T. Kiehl, J. F. Müller, T. Schneider, C. Granier, X. Tie, and D. Hauglustaine, Past and future changes in global tropospheric ozone: Impact on radiative forcing, *Geophys. Res. Lett.*, 25, 3807-3810, 1998.

Brown, S. S., R. K. Talukdar, and A. R. Ravishankara, Reconsideration of the rate constant for the reaction of hydroxyl radicals with nitric acid, *J. Phys. Chem.*, 103, 3031-3037, 1999.

Chin, M., D. J. Jacob, G. M. Gardner, M. S. Forman-Fowler, P. A. Spiro, and D. L. Savoie, A global three-dimensional model of tropospheric sulfate, *J. Geophys. Res.*, 101, 18,667-18,690, 1996.

Collins, W. J., D. S. Stevenson, C. E. Johnson, and R. G. Derwent, Tropospheric ozone in a global-scale three-dimensional Lagrangian model and its response to NOx emission controls, *J. Atmos. Chem.*, 26, 223-274, 1997.

Connors, V. S., B. B. Gormsen, S. Nolf, and H. G. Reichle, Spaceborne observations of the global distribution of carbon monoxide in the middle troposphere during April and October 1994, *J. Geophys. Res.*, 104, 21455-21470, 1999.

Crutzen, P. J., M. G. Lawrence, and U. Poschl, On the background photochemistry of tropospheric ozone, *Tellus*, 51A-B, 123-146, 1999.

Del Genio, A. D. and M-S. Yao, Efficient cumulus parameterization for long-term climate studies: the GISS scheme. In The Representation of Cumulus Convection in Numerical Models, (K. Emanuel and D. Raymond, Eds.), *A M S Monograph Series*. No. 46, 181-184, 1993.

Del Genio, A., M.-S. Yao, W. Kovari, and K.K.-W. Lo, A prognostic cloud water parameterization for global climate models, *J. Climate*, 9, 207-304, 1996.

Dentener, F. J., and P. J. Crutzen, Reaction of N2O5 on tropospheric aerosols,: Impact on the global distributions of NOx, O3 and OH, *J. Geophys. Res.*, 98, 7149-7163, 1993.

Friedl, R. (ed.), Atmospheric effects of subsonic aircraft: Interim assessment report of the advanced subsonic technology program, NASA reference publ. 1400, 143pp, 1997.

Fuglestvedt, J. S., I. S. A. Isaksen, and W.-C. Wang, Estimates of indirect global warming potentials for CH4, CO and NOx, *Climatic Change*, 34, 405-437, 1996.

Gettelman, A., J. R. Holton, and K. H. Rosenlof, Mass fluxes of O3, CH4, N2O, and CF2Cl2 in the lower stratosphere calculated from observational data, *J. Geophys. Res.*, 102, 19,149-19,159, 1997.

Graustein, W. C., and K. K. Turekian, 7Be and 210Pb indicate an upper troposphere source for elevated ozone in the summertime subtropical free troposphere of the eastern North Atlantic, *Geophys. Res. Lett.*, 23, 539-542, 1996.

Grenfell, J. L., D. T. Shindell, D. Koch, D. Rind, C. Price, V. Grewe, and L. J. Mickley, Chemistry-climate interactions in the GISS GCM. Part II: New insights into modeling the pre-industrial atmosphere, in preparation, *J. Geophys. Res.*.

Grewe, V., D. Brunner, M. Dameris, J. L. Grenfell, R. Hein, D. Shindell, and J. Staehelin, Origin and variability of upper tropospheric nitrogen oxides and ozone at northern mid-latitudes, submitted to Atm. Env., 2000.

Hansen, J., G. Russell, D. Rind, P. Stone, A. Lacis, S. Lebedeff, R. Ruedy, and L. Travis, Efficient three-dimensional global models for climate studies: Models I and II, *Mon. Wea. Rev.*, 111, 609-662, 1983.

Hansen, J., et al., A Pinatubo climate investigation. in *The Effects of M. Pinatubo Eruption on the Atmosphere and Climate*, NATO ASI Series Subseries 1 *Global Environment Change*, eds. G. Fiocco, D. Fua, and G. Visconti. Springer-Verlag, publisher, 1996.

Hansen, J., M. Sato, A. Lacis, R. Ruedy, I. Tegen, and E. Matthews, Climate forcings in the Industrial era, *Proc. Natl. Acad. Sci.*, 95, 12,753-12,758, 1998.

Hauglustaine, D. A., C. Granier, G. P. Brasseur, and G. Megie, The importance of atmospheric chemistry in the calculation of radiative forcing on the climate system, *J. Geophys. Res.*, 99, 1173-1186, 1994.

Hauglustaine, D. A., G. P. Brasseur, S. Walters, P. J. Rasch, J. F. Müller, L. K. Emmons, and M. A. Carroll, MOZART: a global chemical transport model for ozone and related chemical tracers, 2, Model results and evaluation, *J. Geophys. Res.*, 103, 28,291-28,335, 1998.

Haywood, J. M., M. D. Schwarzkopf, and V. Ramaswamy, Estimates of radiative forcing due to modeled increases in tropospheric ozone, *J. Geophys. Res.*, 103, 16,999-17,007, 1998.

Horowitz, L. W., J. Liang, G. M. Gardner, and D. J. Jacob, Export of reactive nitrogen from North America during summertime: Sensitivity to hydrocarbon chemistry, *J. Geophys. Res.*, 103, 13451-13476, 1998.

Houweling, S., F. Dentener, and J. Lelieveld, The impact of non-methane hydrocarbon compounds on tropospheric photochemistry, *J. Geophys. Res.*, 103, 10,673-10,696, 1998.

International Panel on Climate Change, Climate Change, 1995, J. T. Houghton, L. G. Meira Filho, B. A. Callander, N. Harris, A. Kattenberg and K. Maskell (eds). Cambridge University Press, Cambridge, England, 572 pp, 1996.

Jaegle, L., et al., Ozone production in the upper troposphere and the influence of aircraft during SONEX: Approach of Nox-saturated conditions, *Geophys. Res. Lett.*, 26, 3081-3084, 1999.

Jeker, D. P., L. Pfister, A. M. Thompson, D. Brunner, D. J. Boccippio, K. E. Pickering, H. Wernli, Y. Kondo, and J. Staehelin, Measurements of nitrogen oxides at the tropopause: Attribution to convection and correlation with lightning, *J. Geophys. Res.*, 105, 3679-3700, 2000.

Kiehl, J. T., T. L. Schneider, R. W. Portmann, and S. Solomon, Climate forcing due to tropospheric and stratospheric ozone, *J. Geophys. Res.*, 104, 31,239-31,254, 1999.

Koch, D., D. Jacob, I. Tegen, D. Rind, and M. Chin, Tropospheric sulfur simulation and sulfate direct radiative forcing in the Goddard Institute for Space Studies general circulation model, *J. Geophys. Res.*, 104, 23,799-23,822, 1999.

Laursen, K. K., P. V. Hobbs, L. F. Radke, and R. A. Rasmussen, Some trace gas emissions from North American biomass fires with an assessment of regional and global fluxes from biomass burning, *J. Geophys. Res.*, 97, 20687-20701, 1992.

Lawrence, M. G., Photochemistry in the tropical Pacific troposphere: Studies with a global 3D chemistry-meteorology model, Doctoral thesis, Ga. Inst. Of Technol., Atlanta, 1996.

Lawrence, M. G., P. J. Crutzen, P. J. Rasch, B. E. Eaton, and N. M. Mahowald, A model for studies of tropospheric photochemistry: Description, global distributions, and evaluation, *J. Geophys. Res.*, 104, 26,245-26,277, 1999.

Lelieveld, J., and F. J. Dentener, What controls tropospheric ozone?, *J. Geophys. Res.*, 105, 3531-3551, 2000.

Levy, H. II, P. S. Kasibhatla, W. J. Moxim, A. A. Klonecki, A. I. Hirsch, S. J. Oltmans, and W. L. Chameides, The global impact of human activity on tropospheric ozone, *Geophys. Res. Lett.*, 24, 791-794, 1997.

Logan, J. A., An analysis of ozonesonde data for the troposphere: Recommendations for testing 3-D models and development of a gridded climatology for tropospheric ozone, *J. Geophys. Res.*, 104, 16,115-16,149, 1999.

Marenco, A., H. Gouget, P. Nedelec, J. P. Pages, and F. Karcher, Evidence of a long-term increase in tropospheric ozone from Pic du Midi data series: Consequences: Positive radiative forcing, *J. Geophys. Res.*, 99, 16,617-16,632, 1994.

Mickley, L. J., P. P. Murti, D. J. Jacob, J. A. Logan, D. M. Koch, and D. Rind, Radiative forcing from tropospheric ozone calculated with a unified chemistry-climate model, *J. Geophys. Res.*, 104, 30,153-30,172, 1999.

Müller, J. F., Geographical distribution and seasonal variation of surface sources and deposition velocities of atmospheric trace gases, *J. Geophys. Res.*, 97, 3787-

3804, 1992.

Müller, J. F., and G. Brasseur, IMAGES: A three-dimensional chemical transport model of the global troposphere, *J. Geophys. Res.*, 100, 16,445-16,490, 1995.

Novelli, P. C., K. A. Masarie, and P. M Lang, Distributions and recent changes in carbon monoxide in the lower troposphere, *J. Geophys. Res.,* 103, 19,015-19,033, 1998.

Olson, J., and coauthors, Results from the intergovernmental panel on climate change photochemical model intercomparison (photocomp), *J. Geophys. Res.*, 102, 5979-5991, 1997.

Parrish, D. D., et al., Relationships between ozone and carbon monoxide at surface sites in the North Atlantic region, *J. Geophys. Res.*, 103, 13357-13376, 1998.

Pickering, K. E., Y. Wang, W-K. Tao, C. Price, and J-F. Müller, Vertical distributions of lightning NOx for use in regional and global chemical transport models, *J. Geophys. Res.*, 103, 31,203-31,216, 1998.

Portmann, R. W., S. Solomon, and B. Briegleb, Radiative forcing of the Earth's climate system due to tropical tropospheric ozone production, *J. Geophys. Res.*, 102, 9409-9425, 1997.

Portmann R. W., S. S. Brown, T. Gierczak, et al., Role of nitrogen oxides in the stratosphere: A reevaluation based on laboratory studies, *Geophys. Res. Lett.*, 26, 2387-2390, 1999.

Prather, M., Numerical advection by conservation of second-order moments, *J. Geophys. Res.*, 91, 6671-6681, 1986.

Price, C., and D. Rind, Possible implications of global climate change on global lightning distributions and frequencies, *J. Geophys. Res.*, 99, 10,823-10,831, 1994.

Price, C., J. Penner, and M. Prather, NOx from lightning, Part 1. Global distribution based on lightning physics, *J. Geophys. Res.*, 102, 5929-5941, 1997.

Prinn, R. G., and A. Golombek, Global atmospheric chemistry of CFC-123, *Nature*, 344, 47-50, 1990.

Prinn, R. G., R. F. Weiss, B. R. Miller, J. Huang, F. N. Alyea, D. M. Cunnold, P. J. Fraser, D. E. Hartley, and P. G. Simmonds, Atmospheric trends and lifetime of CH3CCl3 and global OH concentrations, *Science*, 269, 187-192, 1995.

Reichle, H. G., et al., Space shuttle based global CO measurements during April and October 1994, MAPS instrument, data reduction, and data validation, *J. Geophys. Res.*, 104, 21443-21454, 1999.

Rind, D., and J. Lerner, Use of on-line tracers as a diagnostic tool in general circulation model development. 1. Horizontal and vertical transport in the troposphere, *J. Geophys. Res.*, 101, 12,667-12,683, 1996.

Rind, D., J. Lerner, K. Shah, and R. Suozzo, Use of on-line tracers as a diagnostic tool in general circulation model development. 2. Transport between the troposphere and stratosphere, *J. Geophys. Res.*, 104, 9151-9167, 1999.

Roelofs, G.-J., and J. Lelieveld, Distribution and budget of O3 in the troposphere calculated with a chemistry general circulation model, *J. Geophys. Res.*, 100, 20,983-20,998, 1995.

Roelofs, G.-J., J. Lelieveld, and R. Van Dorland, A three-dimensional chemistry/general circulation model simulation of anthropogenically derived ozone in the troposphere and its radiative forcing, *J. Geophys. Res.*, 102, 23,389-23,401, 1997.

Schumann, U., H. Schlager, F. Arnold, J. Ovarlez, H. Kelder, O. Hov, G. Hayman, I. S. Isaksen, J. Staehelin, and P. D. Whitefield, Pollution from aircraft emissions in the North Atlantic flight corridor: Overview on the POLINAT projects, *J. Geophys. Res.*, 105, 3605-3631, 2000.

Shine, K. P., et al., Radiative forcing due to changes in ozone: A comparison of different codes, in Atmospheric Ozone as a Climate Gas, edited by W. C. Wang and I. S. Isaksen, pp. 373-396, Springer-Verlag, New York, 1995.

Stevenson, D. S., C. E. Johnson, W. J. Collins, R. G. Derwent, K. P. Shine, and J. M. Edwards, Evolution of tropospheric radiative forcing, *Geophys. Res. Lett.*, 25, 3819-3822, 1998.

Stevenson, D. S., C. E. Johnson, W. J. Collins, R. G. Derwent, and J. M. Edwards, Future tropospheric ozone radiative forcing and methane turnover - the impact of climate change, *Geophys. Res. Lett.*, submitted, 2000.

Thompson, A. M., The oxidizing capacity of the Earth's atmosphere: probable past and future changes, *Science*, 256, 1157-1165, 1992.

Trainer, M., D. D. Parrish, and M. P. Buhr, Correlation of ozone with NOy in photochemically aged air, *J. Geophys. Res.*, 98, 2917-2932, 1993.

van Dorland, R., F. J. Dentener, and J. Lelieveld, Radiative forcing due to tropospheric ozone and sulfate aerosol, *J. Geophys. Res.*, 102, 28,079-28,100, 1997.

Wang, Y., and D. Jacob, Anthropogenic forcing of tropospheric ozone and OH since preindustrial times, *J. Geophys. Res.*, 103, 31,123-31,135, 1998.

Wang, Y., D. Jacob, and J. Logan, Global simulation of tropospheric O3-NOx -hydrocarbon chemistry 1. Model formulation, *J. Geophys. Res.*, 103, 10,713-10,725, 1998a.

Wang, Y., D. Jacob, and J. Logan, Global simulation of tropospheric O3-NOx -hydrocarbon chemistry 2. Model evaluation and global ozone budget, *J. Geophys. Res.*, 103, 10,727-10,755, 1998b.

Wang, Y., D. Jacob, and J. Logan, Global simulation of tropospheric O3-NOx -hydrocarbon chemistry 3. Origin of tropospheric ozone and effects of nonmethane hydrocarbons, *J. Geophys. Res.*, 103, 10,757-10,767, 1998c.

Wesely, M. L., and B. B. Hicks, Some factors that affect the deposition rates of sulfur dioxide and similar gases on vegetation, *J. Air Pollut. Control Assoc.*, 27, 1110-1116, 1977.

World Meteorological Organization, *Scientific assessment of ozone depletion: 1994*, Rep. 37, Global Ozone Res. and Monit. Proj., Geneva, 1994.

World Meteorological Organization, *Scientific assessment of ozone depletion: 1998*, Rep. 44, Global Ozone Res. and Monit. Proj., Geneva, 1999.

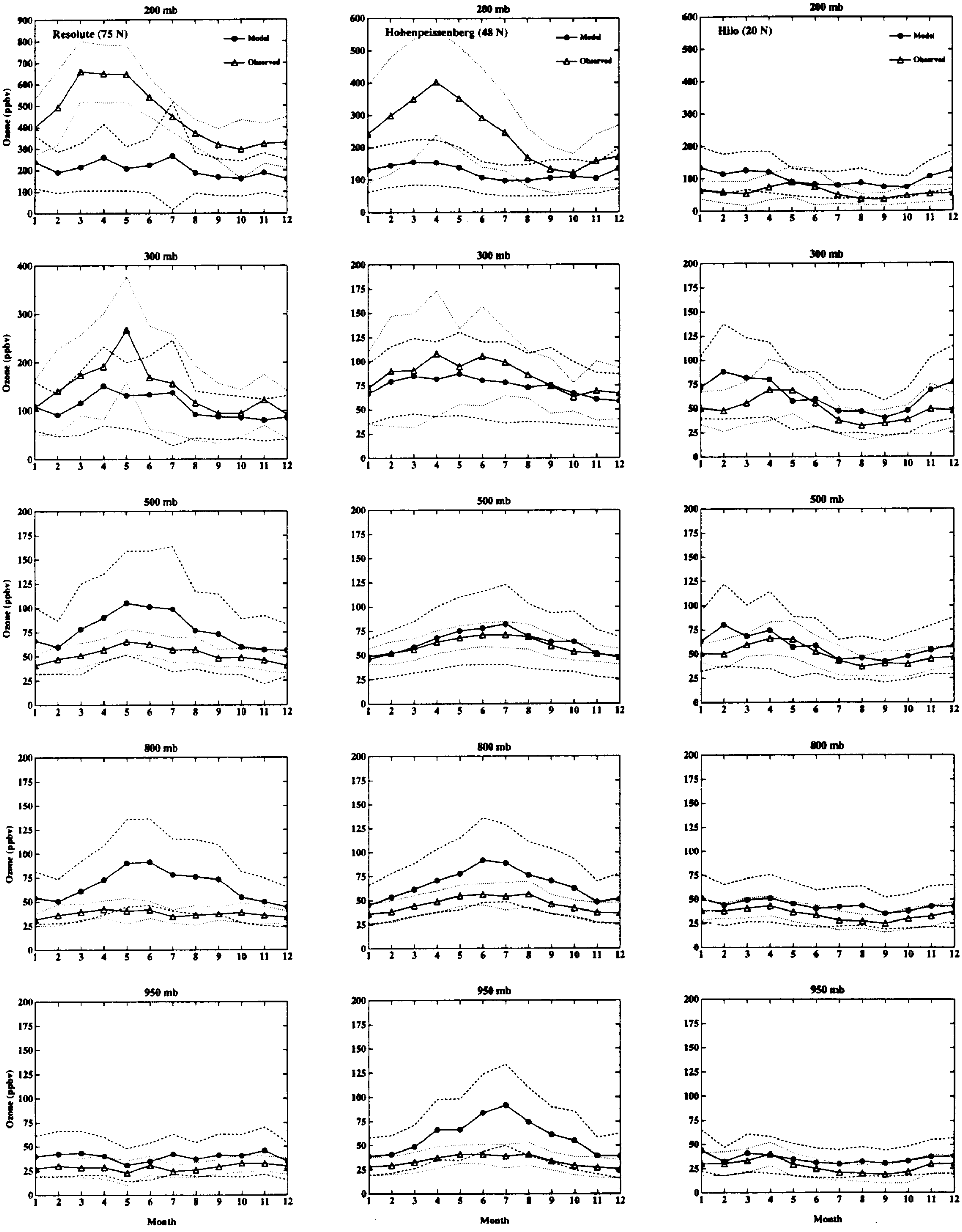
200 mb
Resolute (75 N)
Model
Observed
Ozone (ppbv)
200 mb
Hohenpeissenberg (48 N)
Model
Observed
200 mb
Hilo (20 N)
Model
Observed
300 mb
300 mb
300 mb
500 mb
500 mb
500 mb
800 mb
800 mb
800 mb
950 mb
950 mb
950 mb
Month
Month
Month

FIG 1
(Part 1)

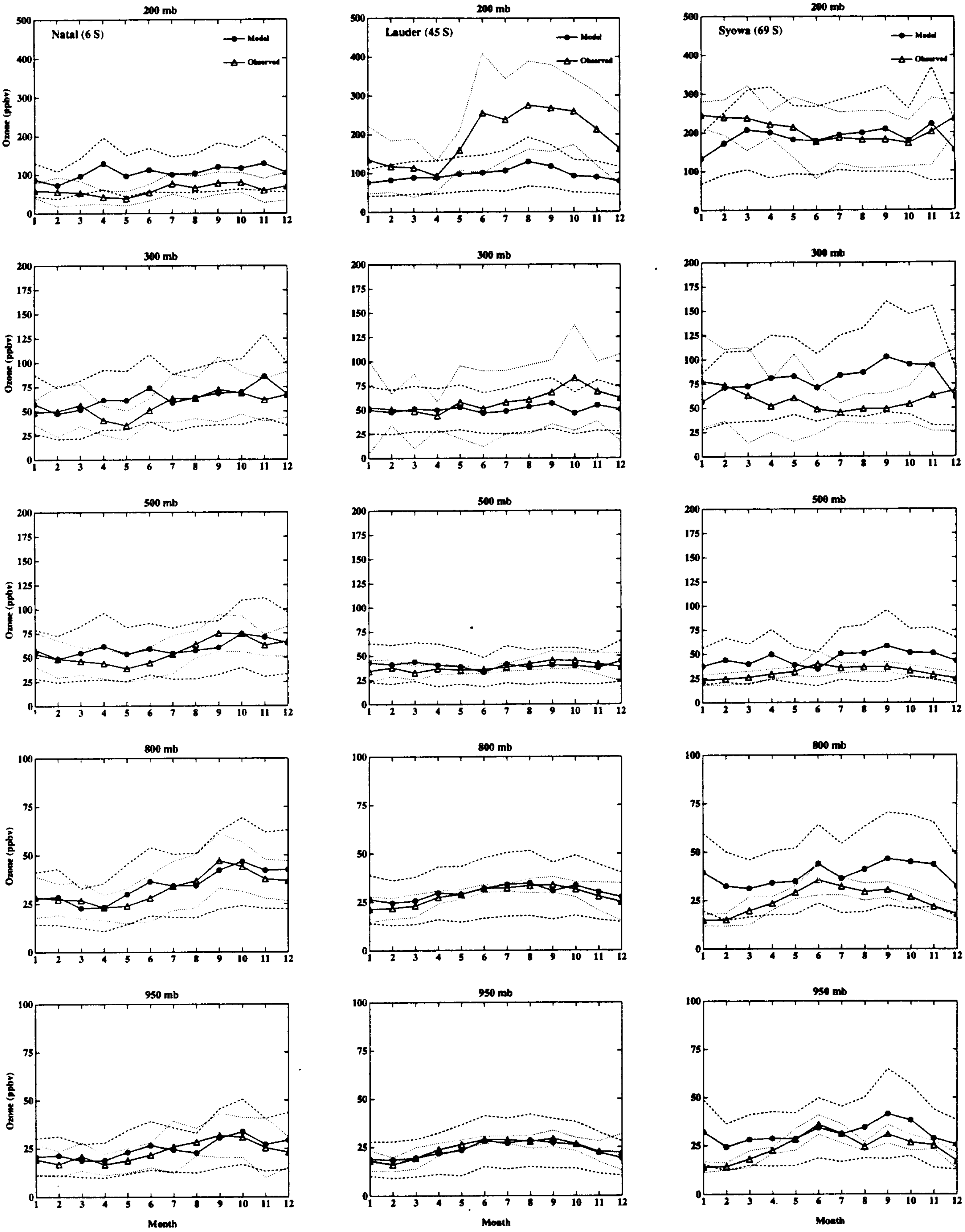
200 mb
Natal (6 S)
Lauder (45 S)
Syowa (69 S)
Model
Observed
300 mb
500 mb
800 mb
950 mb
Ozone (ppbv)
Month
1 2 3 4 5 6 7 8 9 10 11 12

FIG 1
(Part 2)

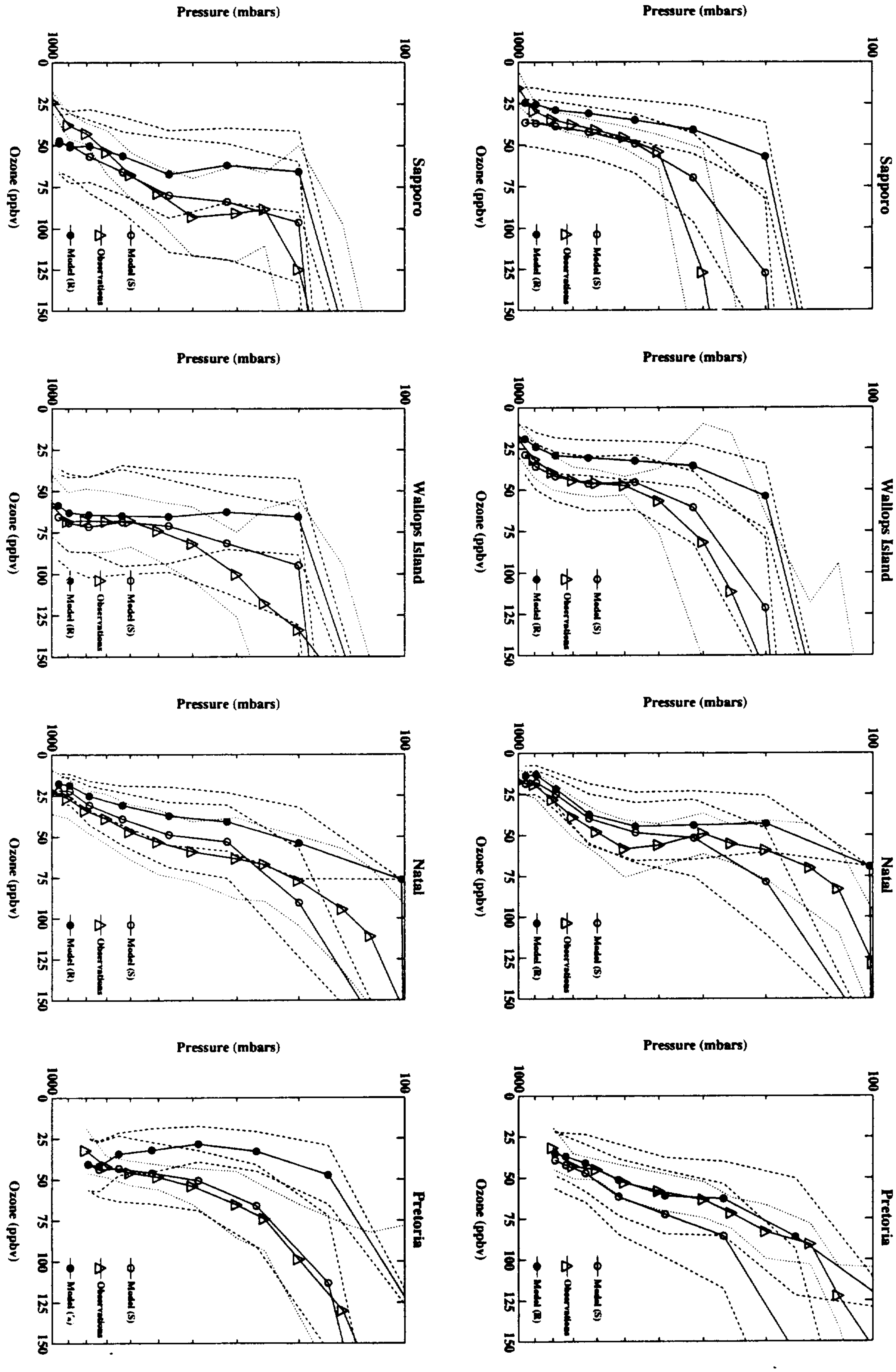
Sapporo
Wallops Island
Natal
Pretoria
Pressure (mbars)
1000
100
Ozone (ppbv)
0
25
50
75
100
125
150
Model (S)
Observations
Model (R)

FIG 2

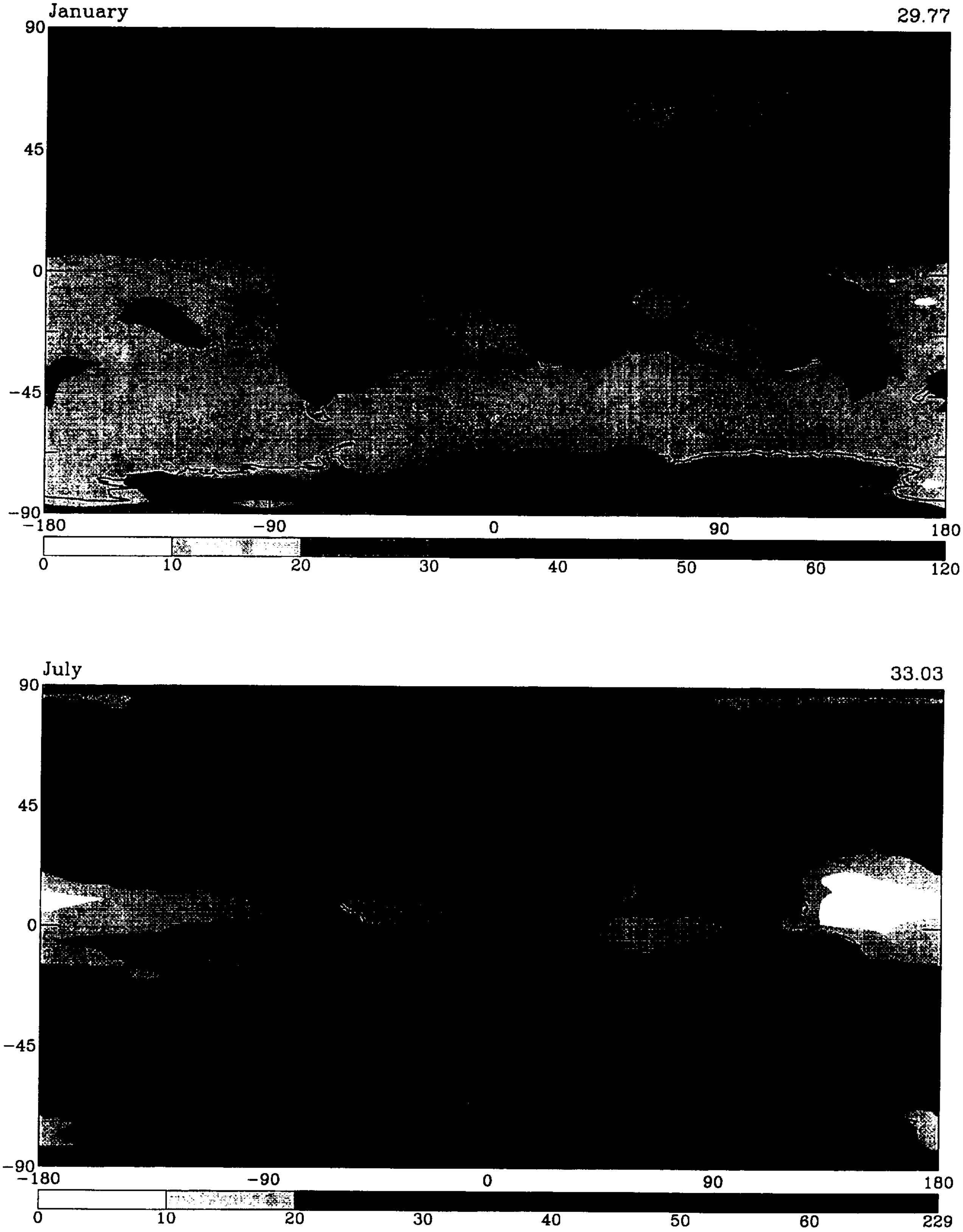
January
29.77
90
45
0
−45
−90
−180
−90
0
90
180
0
10
20
30
40
50
60
120
July
33.03
90
45
0
−45
−90
−180
−90
0
90
180
0
10
20
30
40
50
60
229

FIG 3

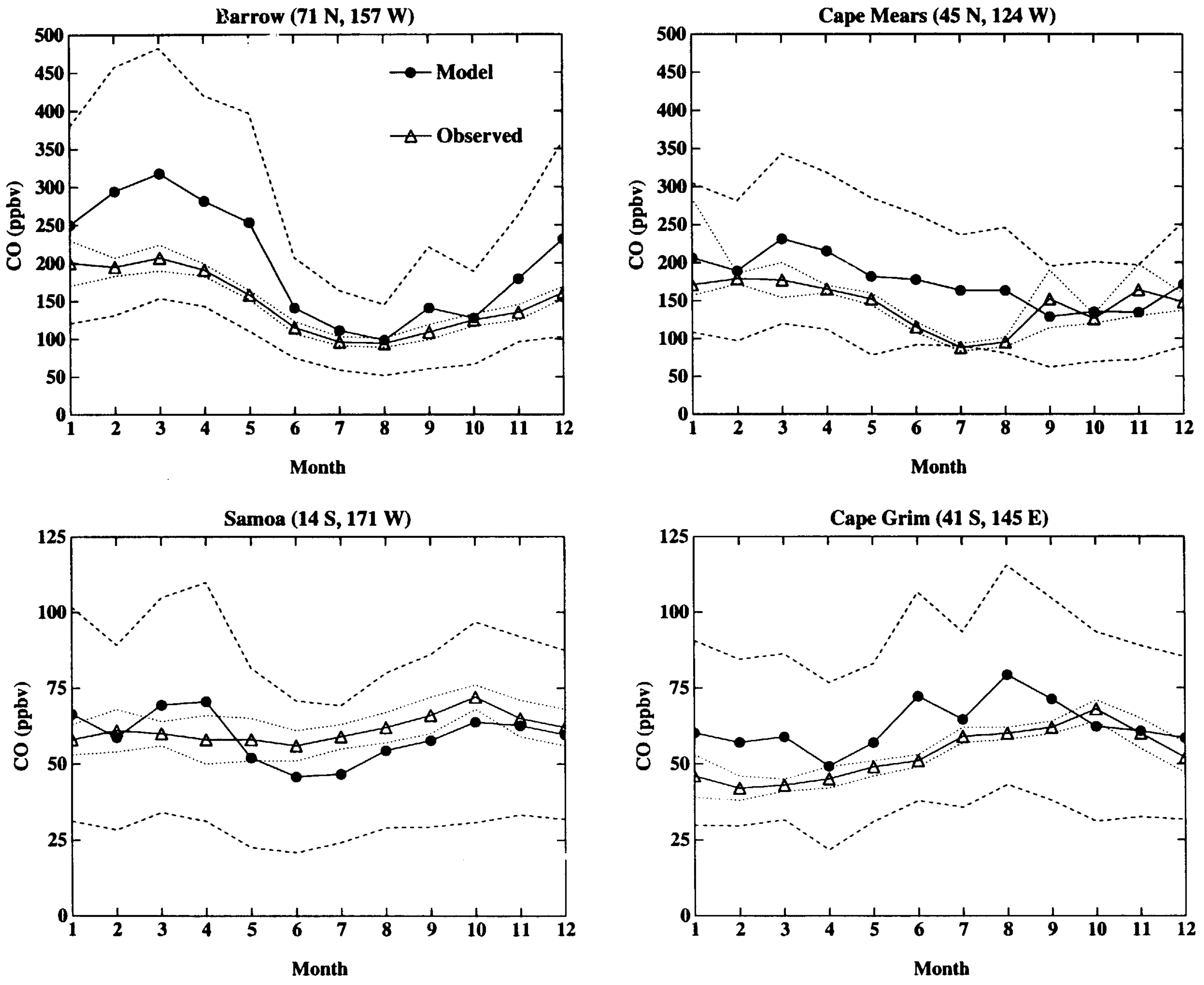
Barrow (71 N, 157 W)
Model
Observed
CO (ppbv)
0
50
100
150
200
250
300
350
400
450
500
Month
1
2
3
4
5
6
7
8
9
10
11
12
Cape Mears (45 N, 124 W)
Samoa (14 S, 171 W)
25
75
125
Cape Grim (41 S, 145 E)

FIG 4

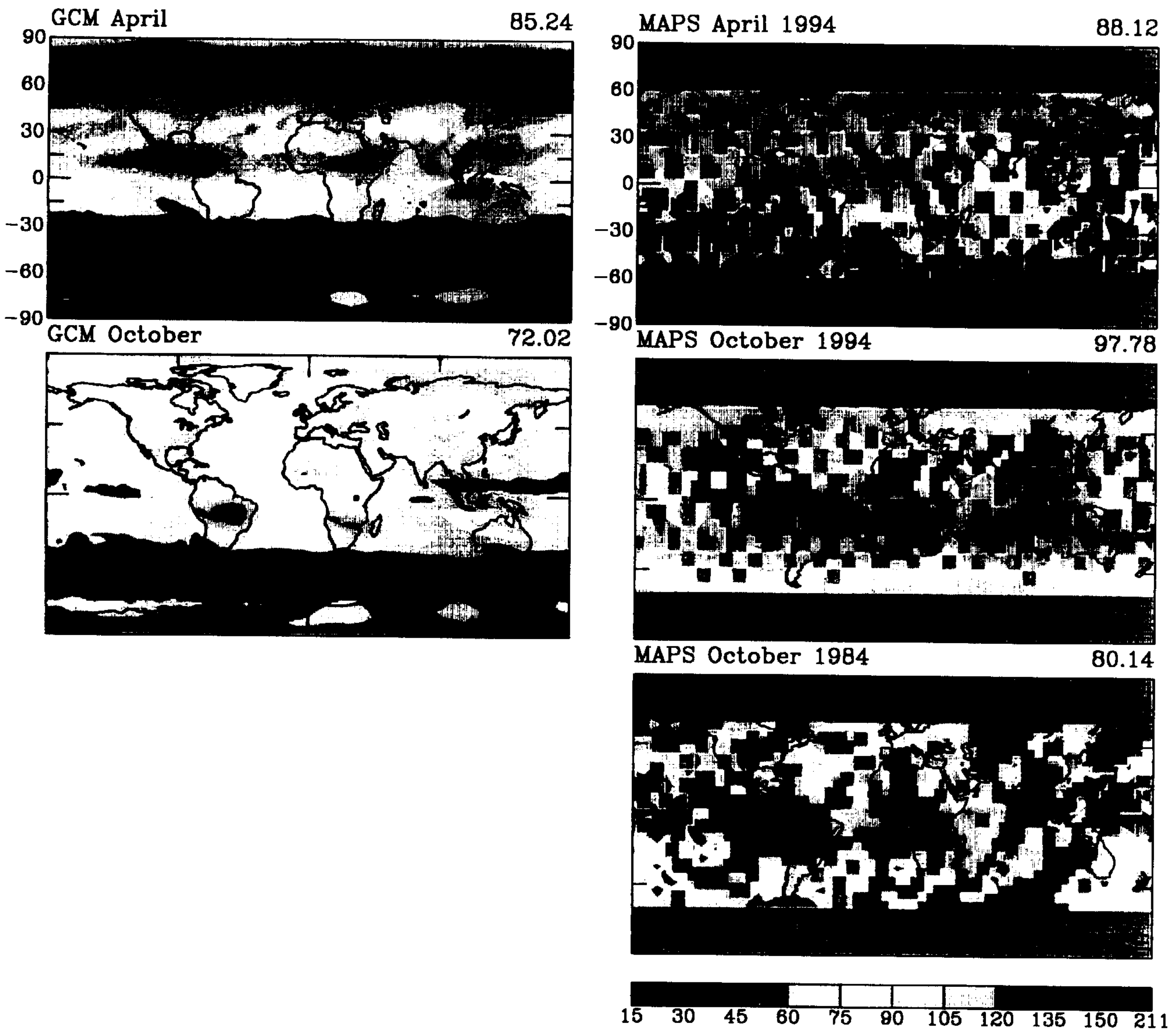
GCM April
85.24
90
60
30
0
−30
−60
−90
GCM October
72.02
MAPS April 1994
88.12
MAPS October 1994
97.78
MAPS October 1984
80.14
15
30
45
60
75
90
105
120
135
150
211

Fig 5

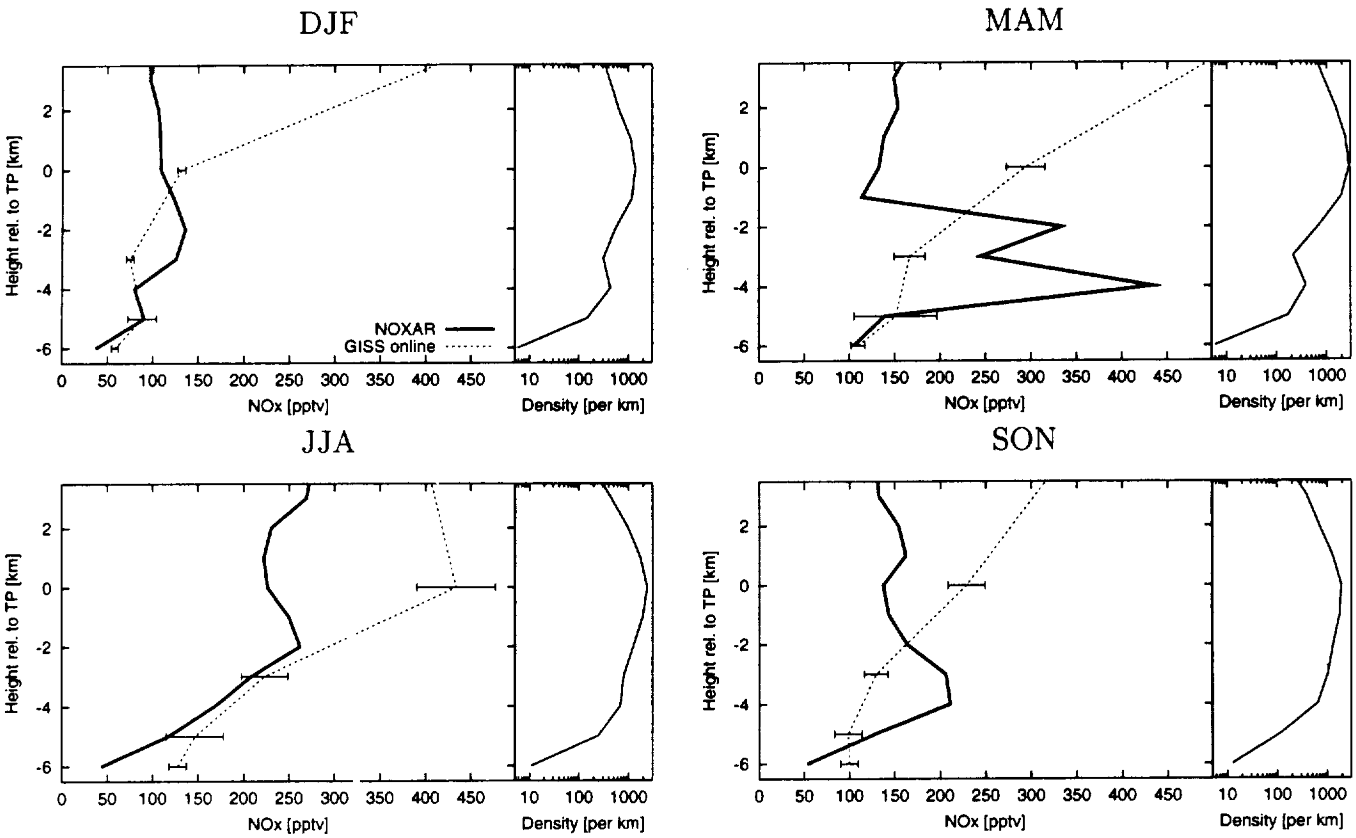
DJF
MAM
JJA
SON
Height rel. to TP [km]
2
0
-2
-4
-6
NOXAR
GISS online
0
50
100
150
200
250
300
350
400
450
NOx [pptv]
10
100
1000
Density [per km]

Fig. 6

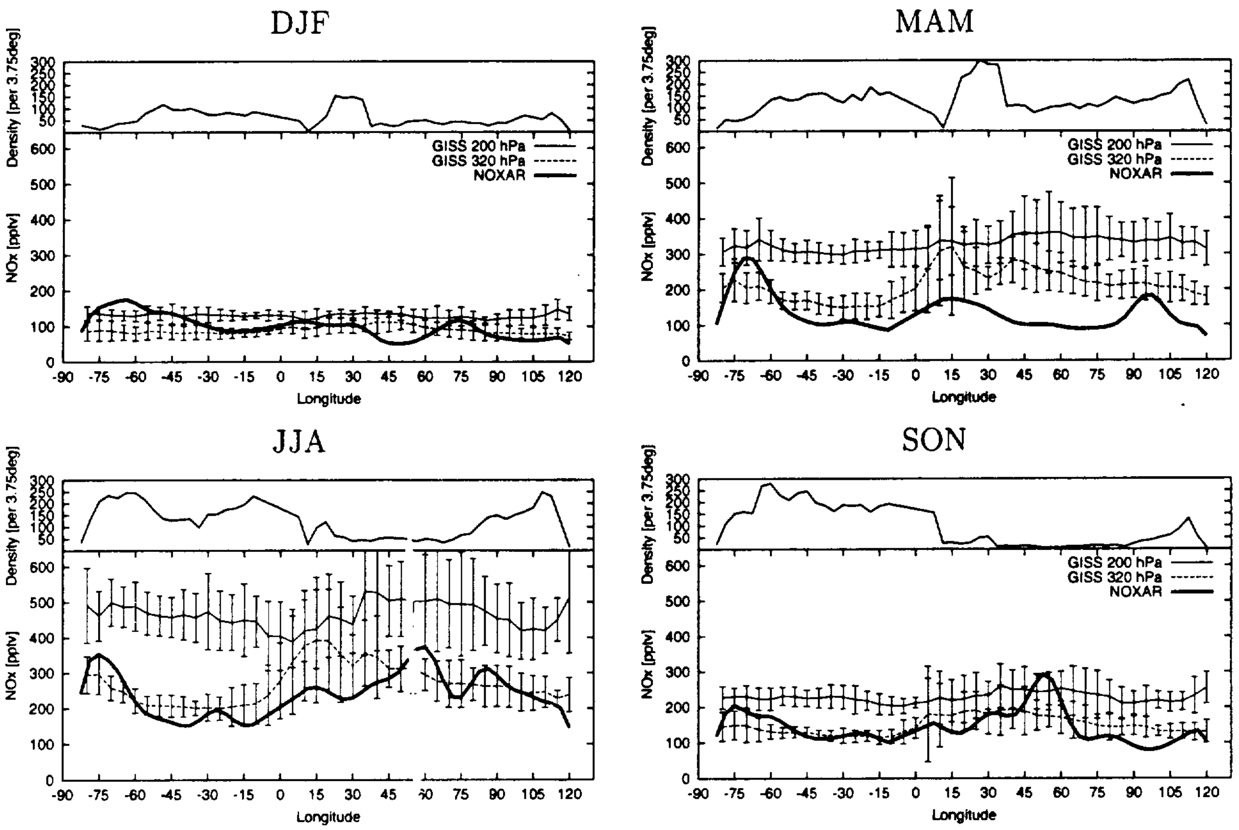
DJF
MAM
JJA
SON
Density [per 3.75deg]
300
250
200
150
100
50
NOx [pptv]
0
100
200
300
400
500
600
GISS 200 hPa
GISS 320 hPa
NOXAR
-90
-75
-60
-45
-30
-15
0
15
30
45
60
75
90
105
120
Longitude

Fig 7

Fig 8

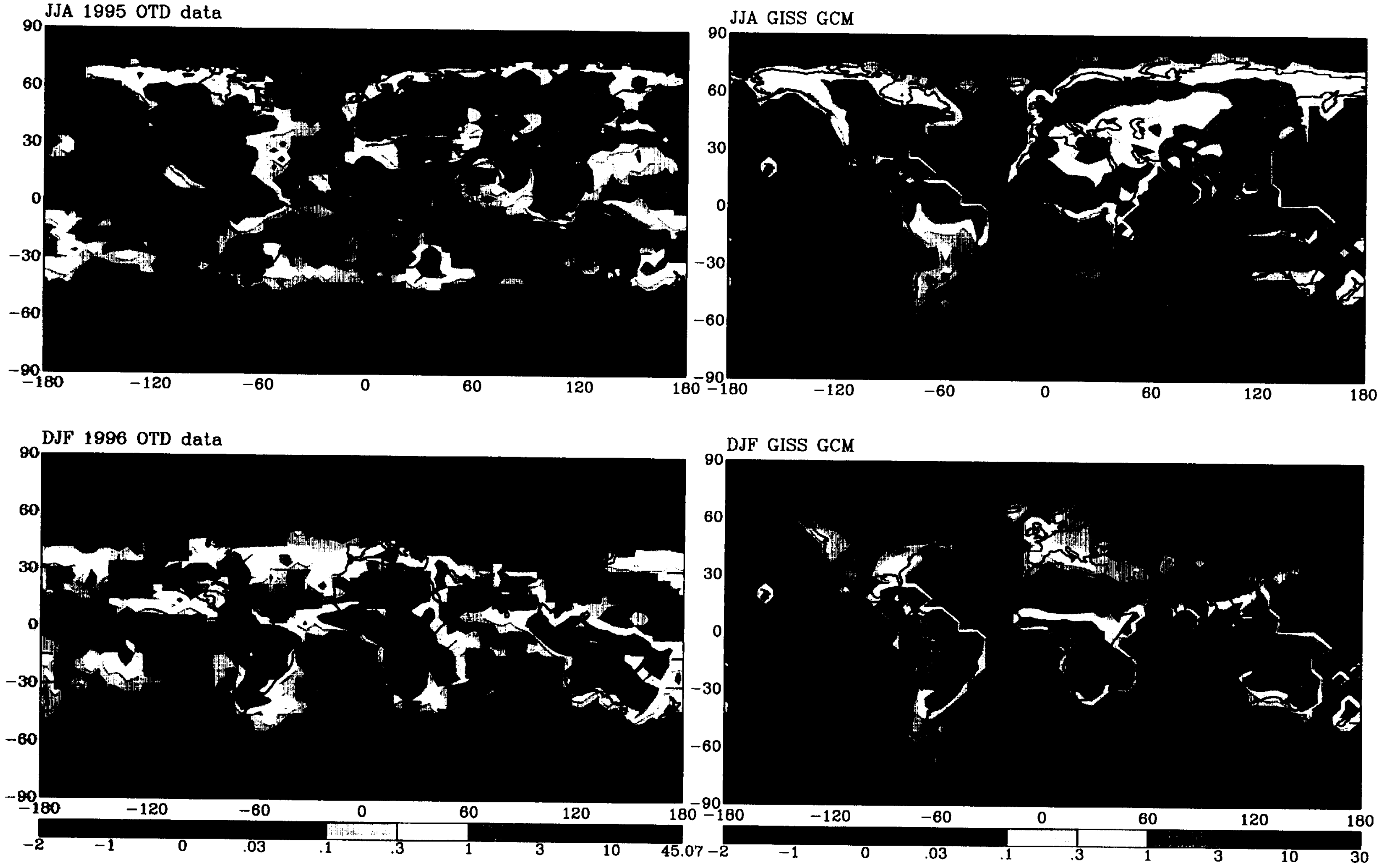
JJA 1995 OTD data
JJA GISS GCM
DJF 1996 OTD data
DJF GISS GCM
90
60
30
0
−30
−60
−90
−180
−120
−60
0
60
120
180
−2
−1
0
.03
.1
.3
1
3
10
45.07
30

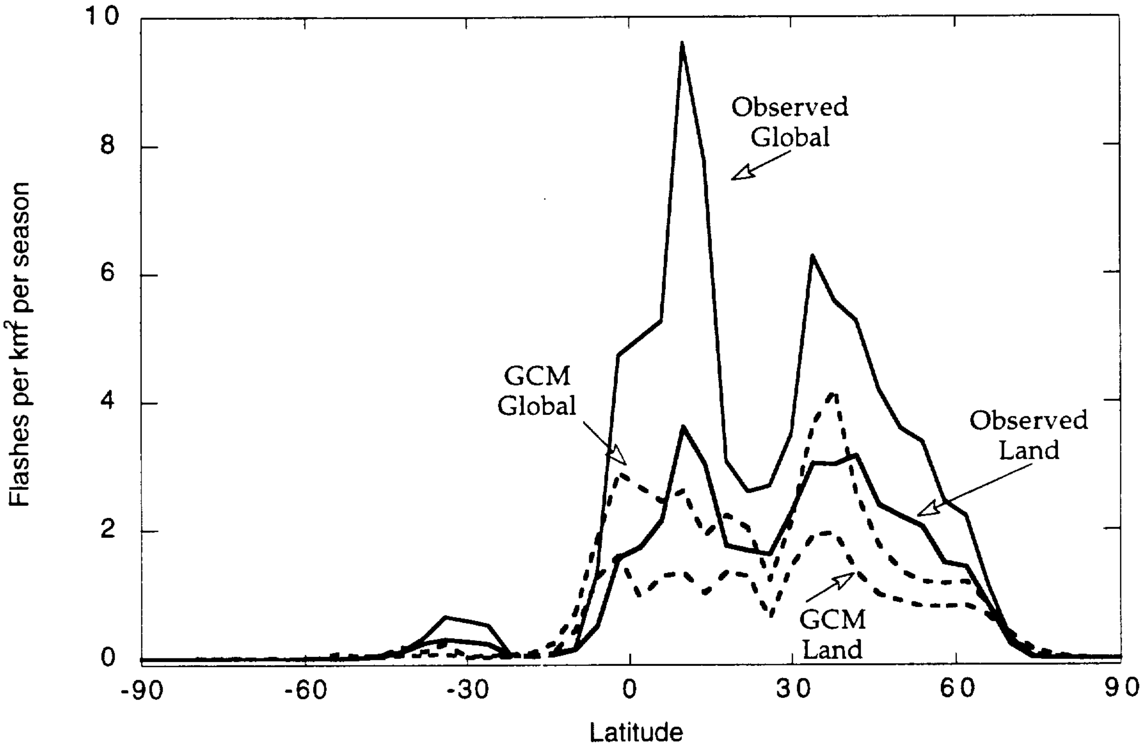

10
8
6
4
2
0
Flashes per km^2 per season
-90
-60
-30
0
30
60
90
Latitude
Observed Global
GCM Global
Observed Land
GCM Land

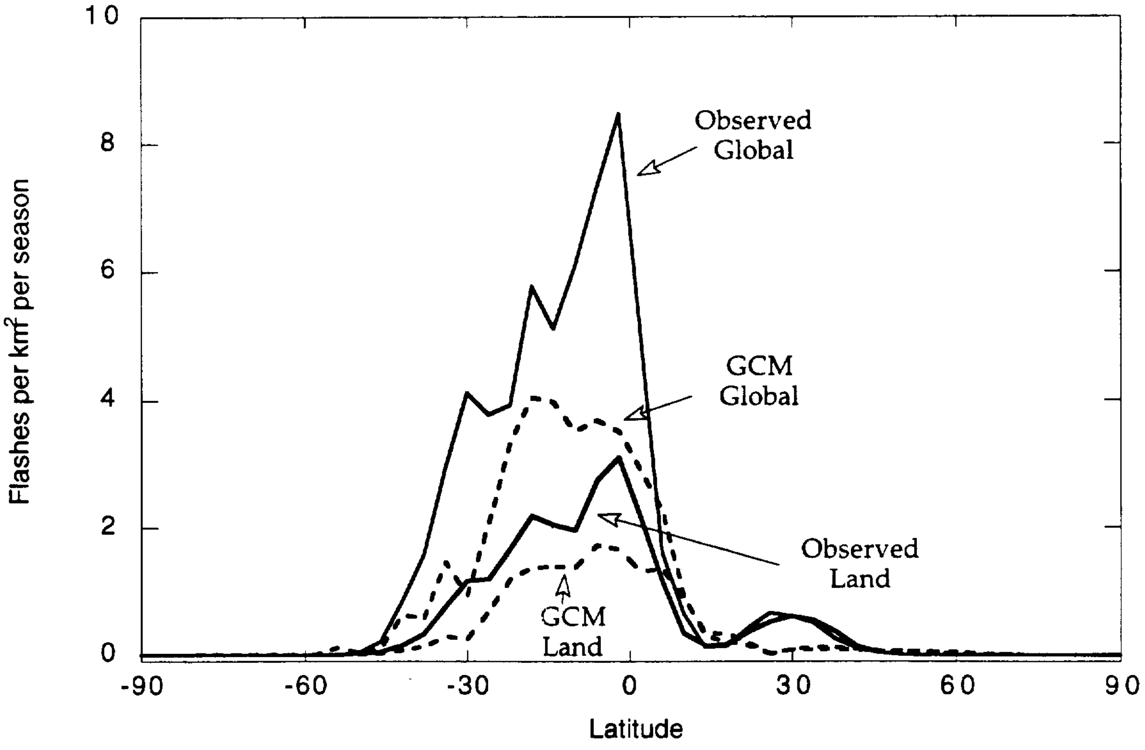

10
8
6
4
2
0
Flashes per km^2 per season
-90
-60
-30
0
30
60
90
Latitude
Observed Global
GCM Global
Observed Land
GCM Land

FIG 9

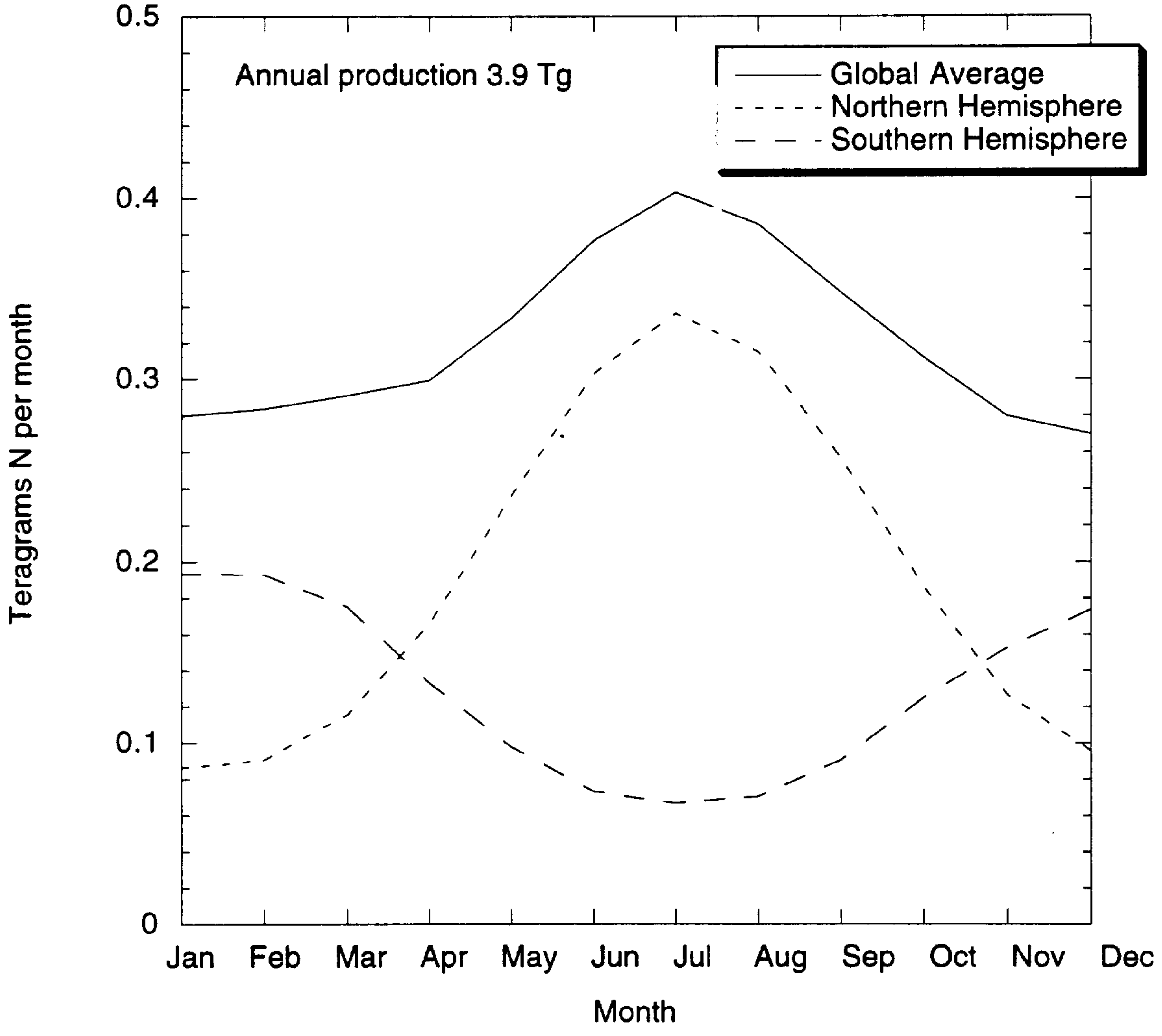

0.5
0.4
0.3
0.2
0.1
0
Annual production 3.9 Tg
Global Average
Northern Hemisphere
Southern Hemisphere
Teragrams N per month
Jan
Feb
Mar
Apr
May
Jun
Jul
Aug
Sep
Oct
Nov
Dec
Month

FIG 10

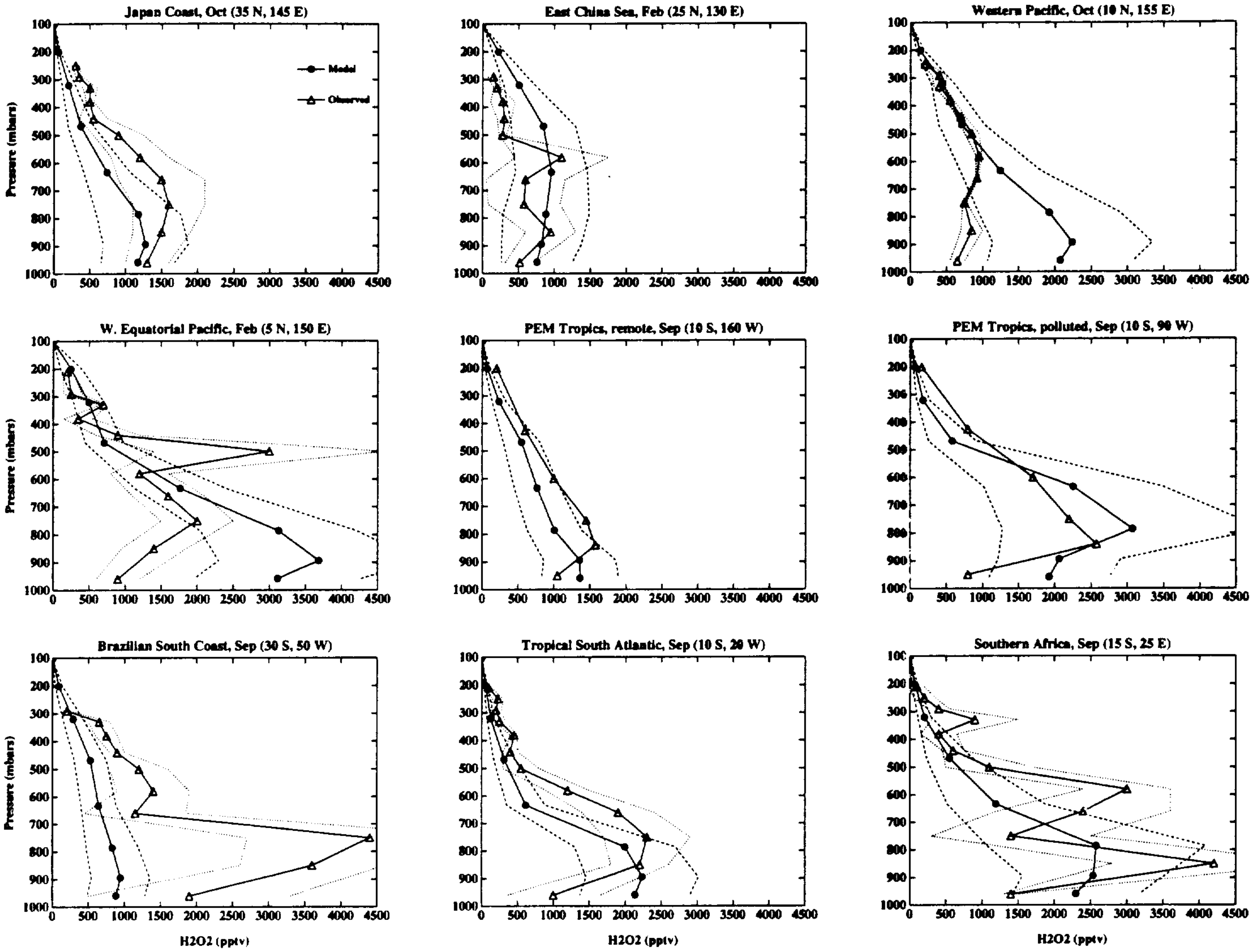
Japan Coast, Oct (35 N, 145 E)
East China Sea, Feb (25 N, 130 E)
Western Pacific, Oct (10 N, 155 E)
W. Equatorial Pacific, Feb (5 N, 150 E)
PEM Tropics, remote, Sep (10 S, 160 W)
PEM Tropics, polluted, Sep (10 S, 90 W)
Brazilian South Coast, Sep (30 S, 50 W)
Tropical South Atlantic, Sep (10 S, 20 W)
Southern Africa, Sep (15 S, 25 E)
Model
Observed
Pressure (mbars)
100
200
300
400
500
600
700
800
900
1000
0
500
1000
1500
2000
2500
3000
3500
4000
4500
H2O2 (pptv)

FIG 11

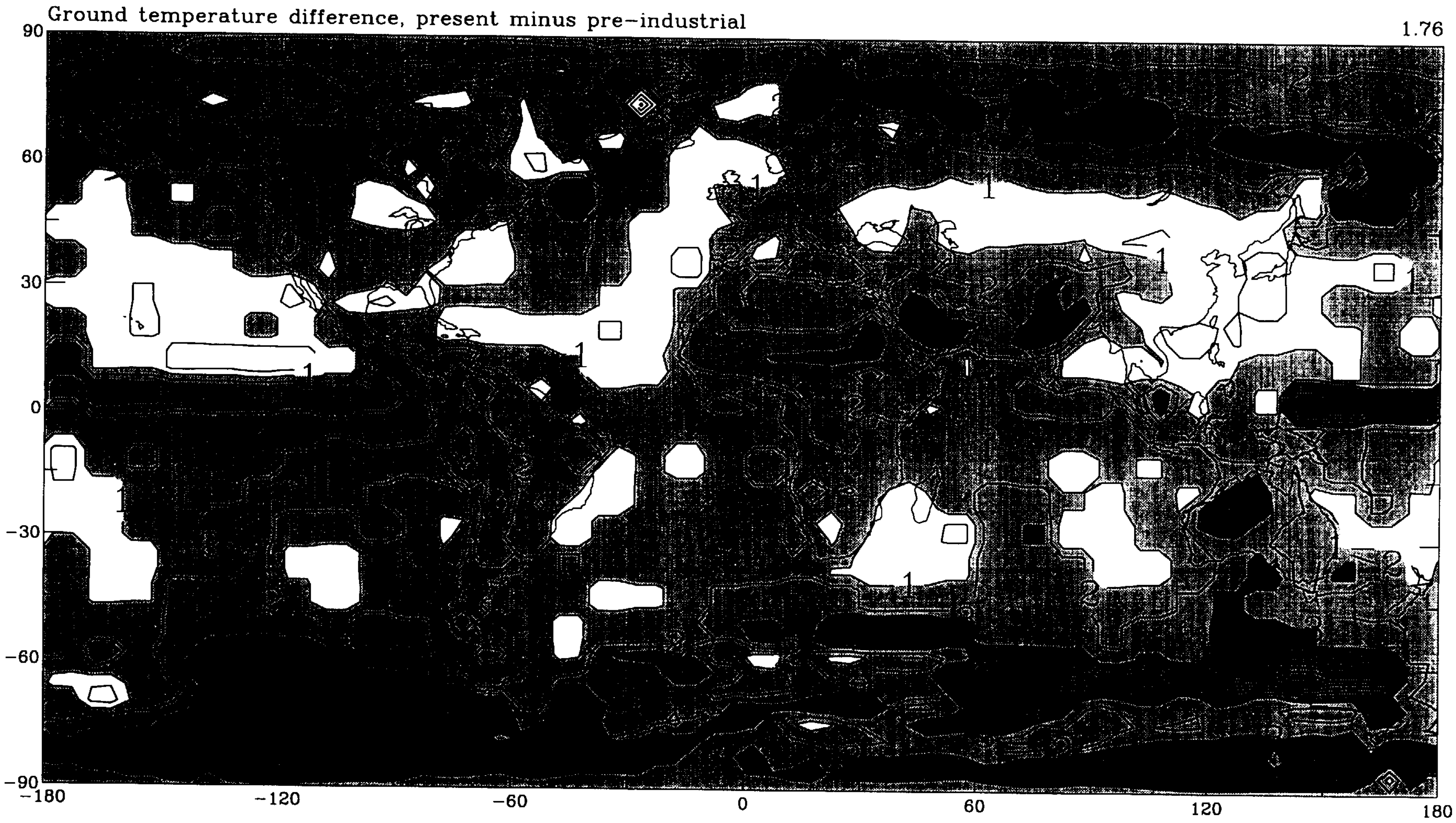
Ground temperature difference, present minus pre−industrial
1.76
90
60
30
0
−30
−60
−90
−180
−120
−60
0
60
120
180
1

FIG 12

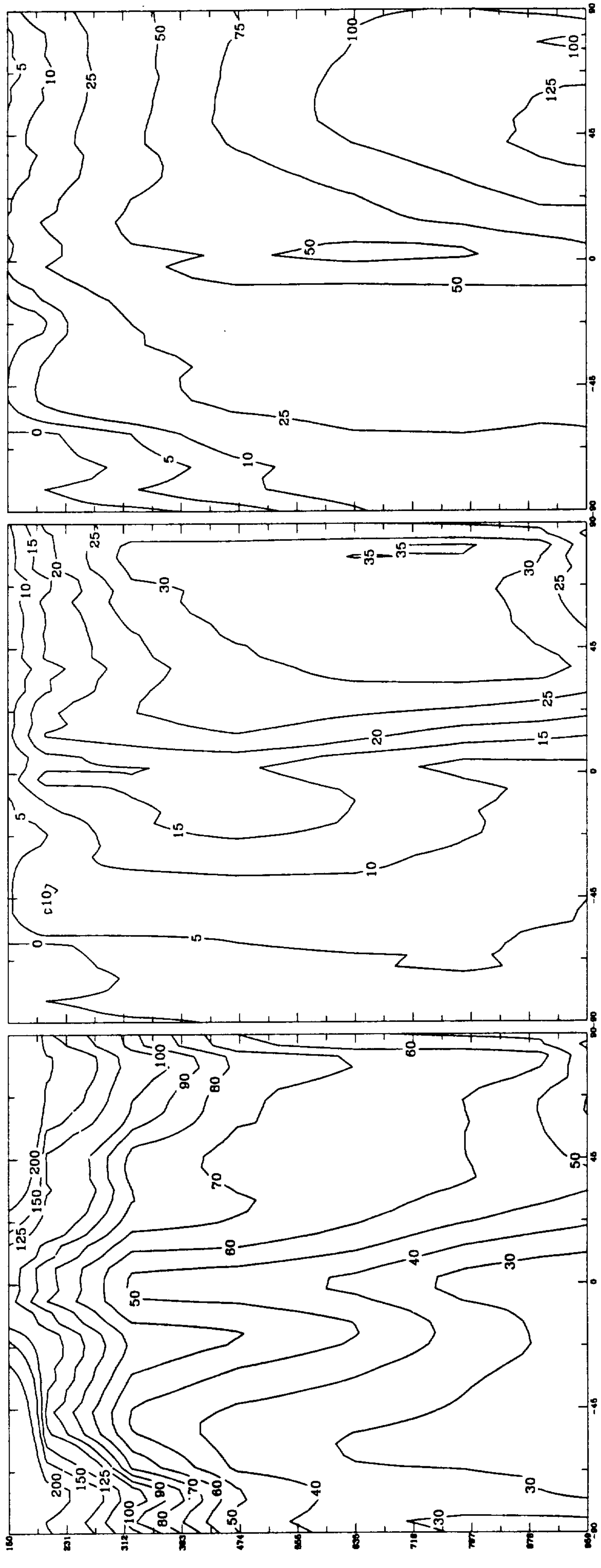
150
231
312
393
474
555
636
718
797
878
959
-90
-45
0
45
90
200
150
125
100
90
80
70
60
50
40
30
c10)
0
5
10
15
20
25
30
35
0
5
10
25
50
75
100
125

FIG 13

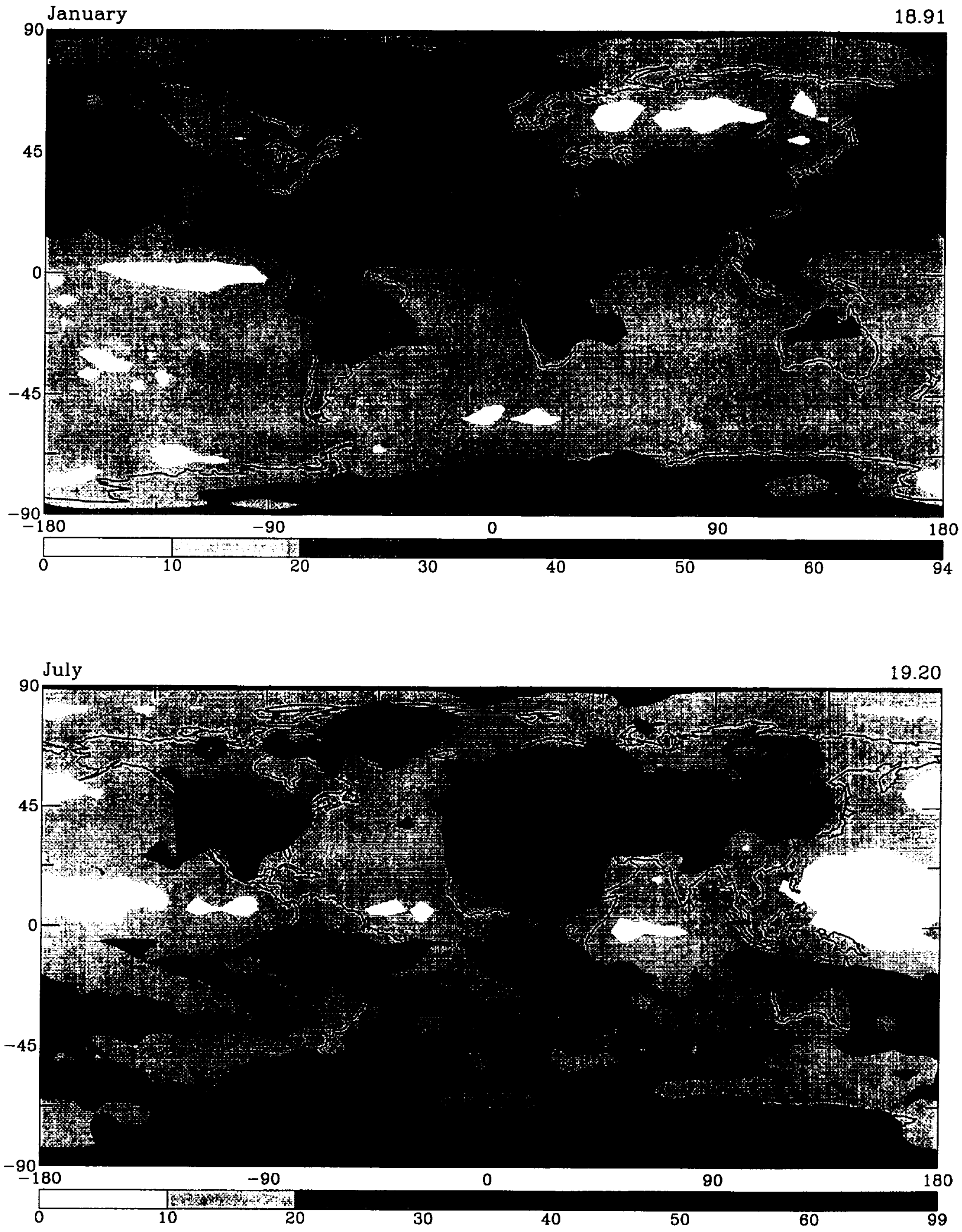
January
18.91
90
45
0
-45
-90
-180
-90
0
90
180
0
10
20
30
40
50
60
94
July
19.20
90
45
0
-45
-90
-180
-90
0
90
180
0
10
20
30
40
50
60
99

FIG 14

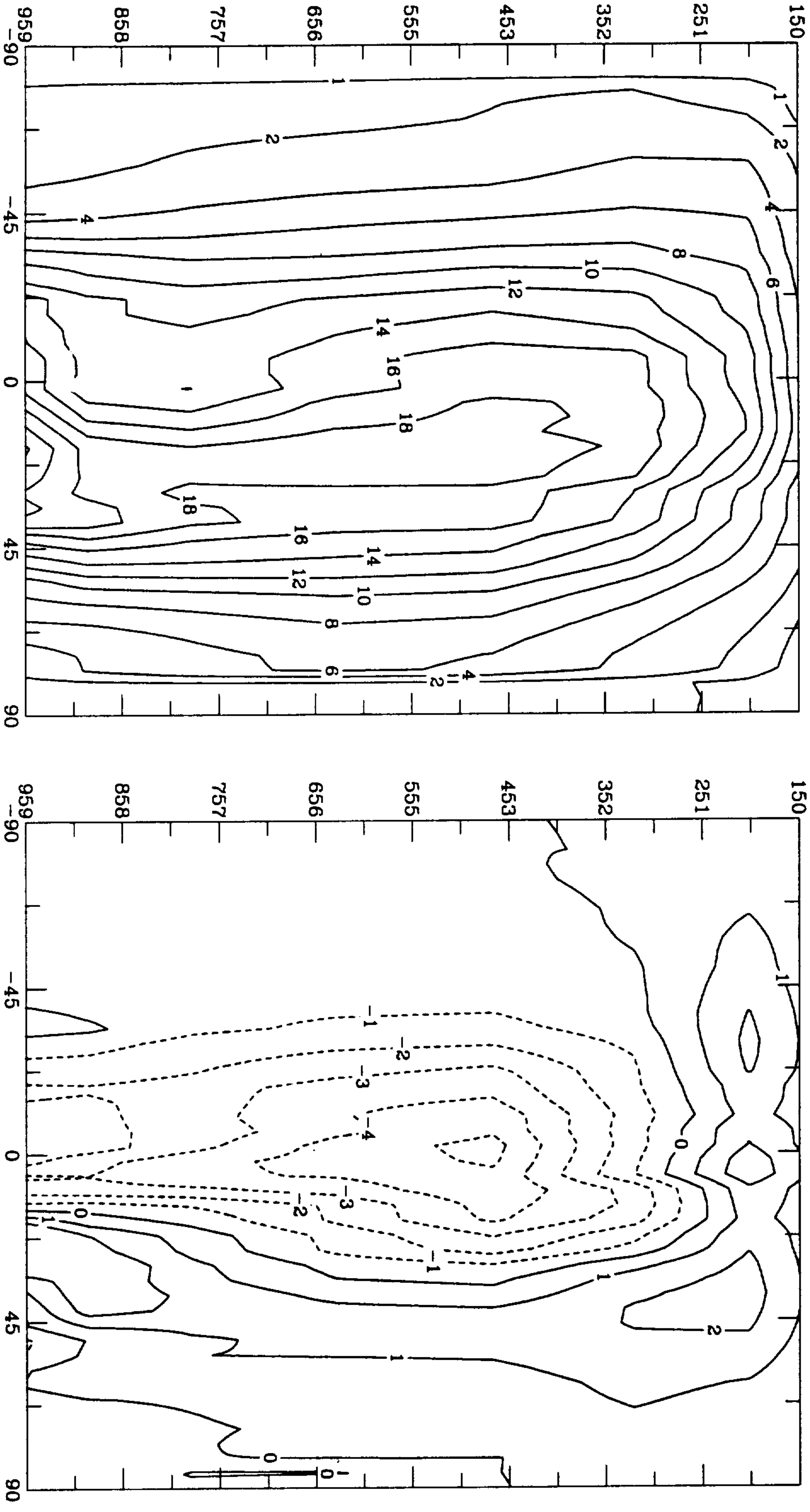

150
251
352
453
555
656
757
858
959
-90
-45
0
45
90
1
2
4
6
8
10
12
14
16
18
-1
-2
-3
-4
0

FIG 15

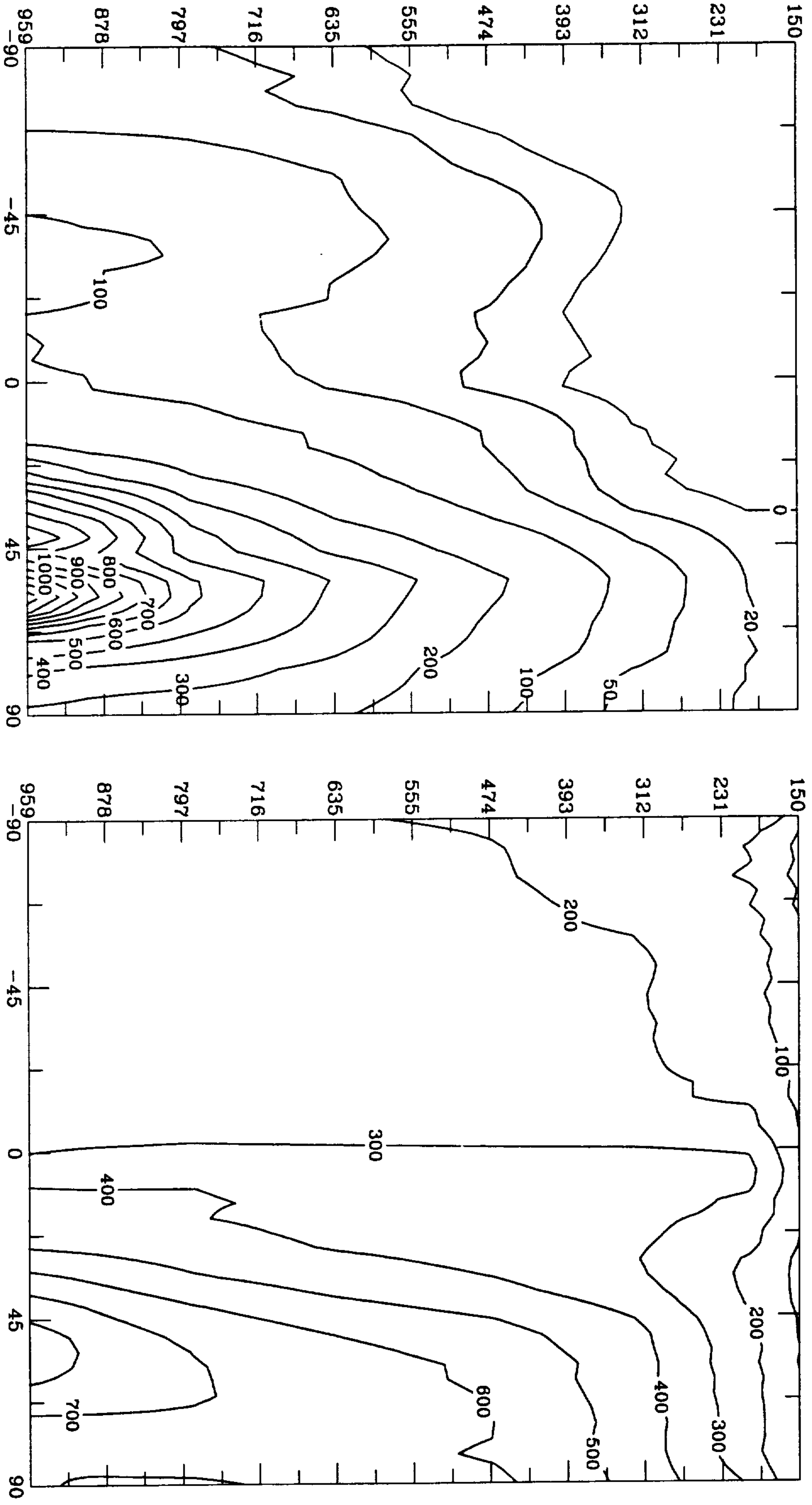

150
231
312
393
474
555
635
716
797
878
959
-90
-45
0
45
90
0
20
50
100
200
300
400
500
600
700
800
900
1000
100
150
231
312
393
474
555
635
716
797
878
959
-90
-45
0
45
90
100
200
300
400
500
600
700

FIG 16

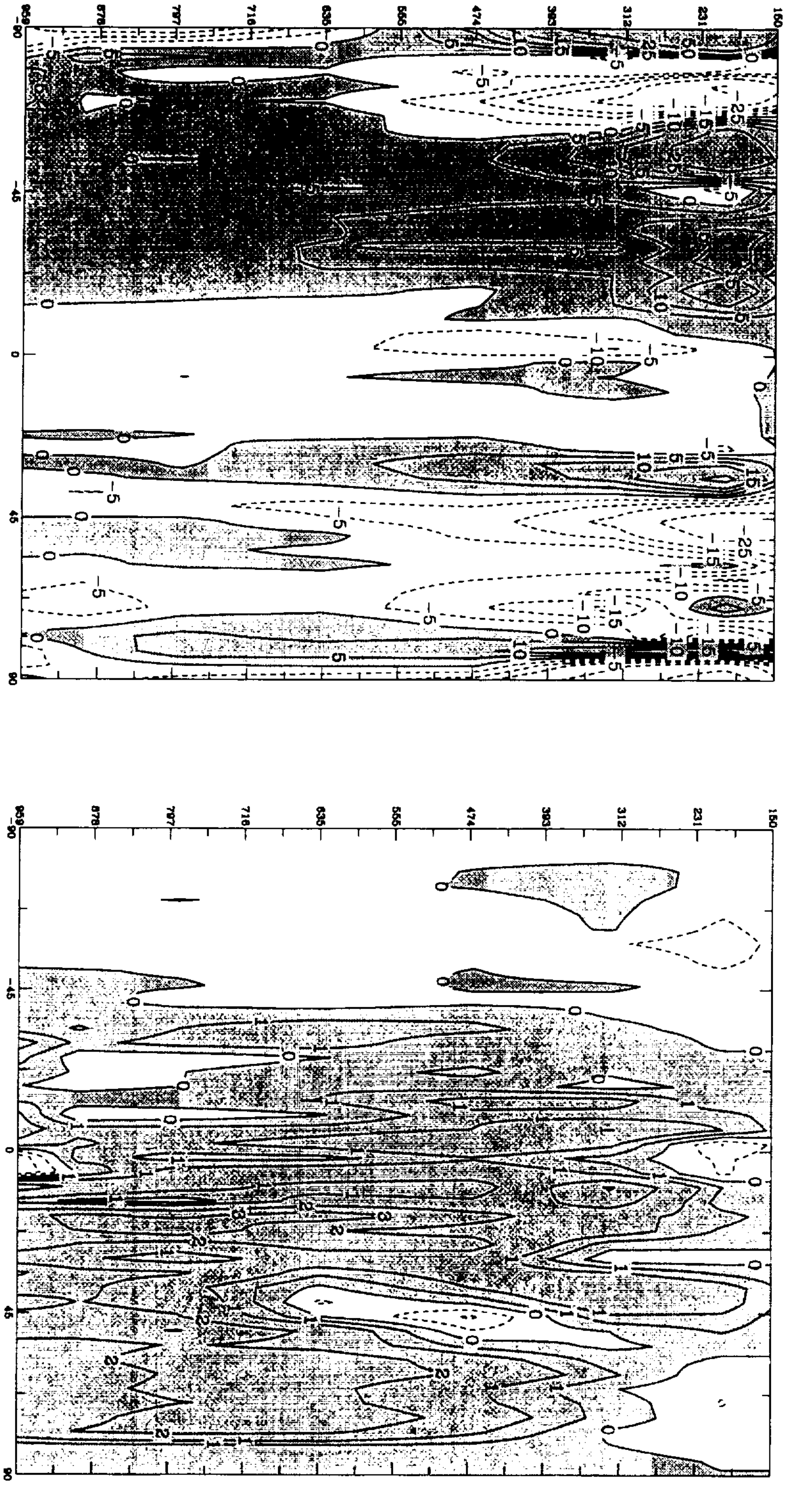

150
231
312
393
474
555
635
716
797
878
959
-90
-45
0
45
90
-25
-15
-10
-5
0
5
10
15
1
2
3

FIG 17

Fig 18

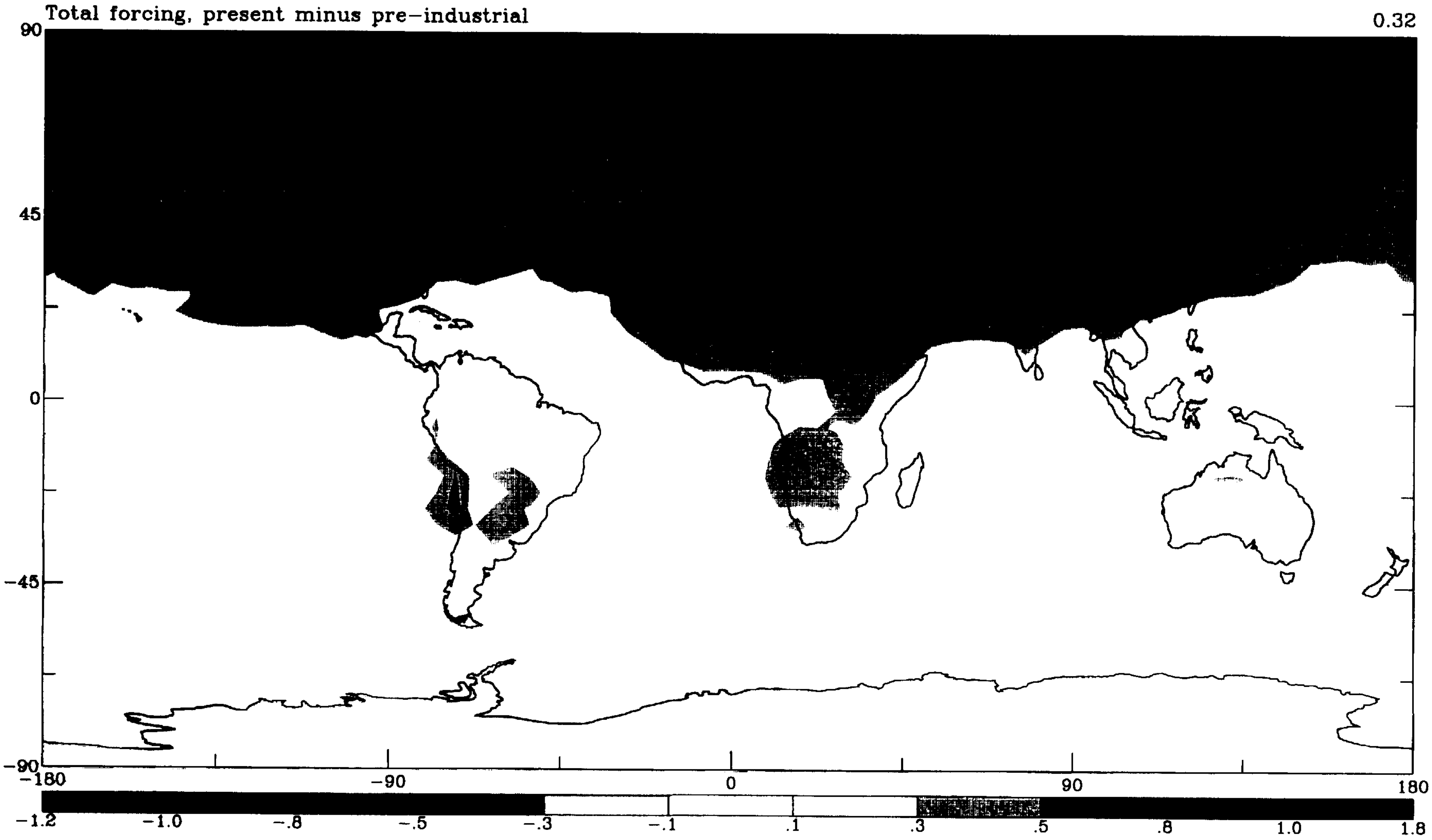

Total forcing, present minus pre-industrial

0.32
90
45
0
-45
-90
-180
-90
0
90
180
-1.2
-1.0
-.8
-.5
-.3
-.1
.1
.3
.5
.8
1.0
1.8

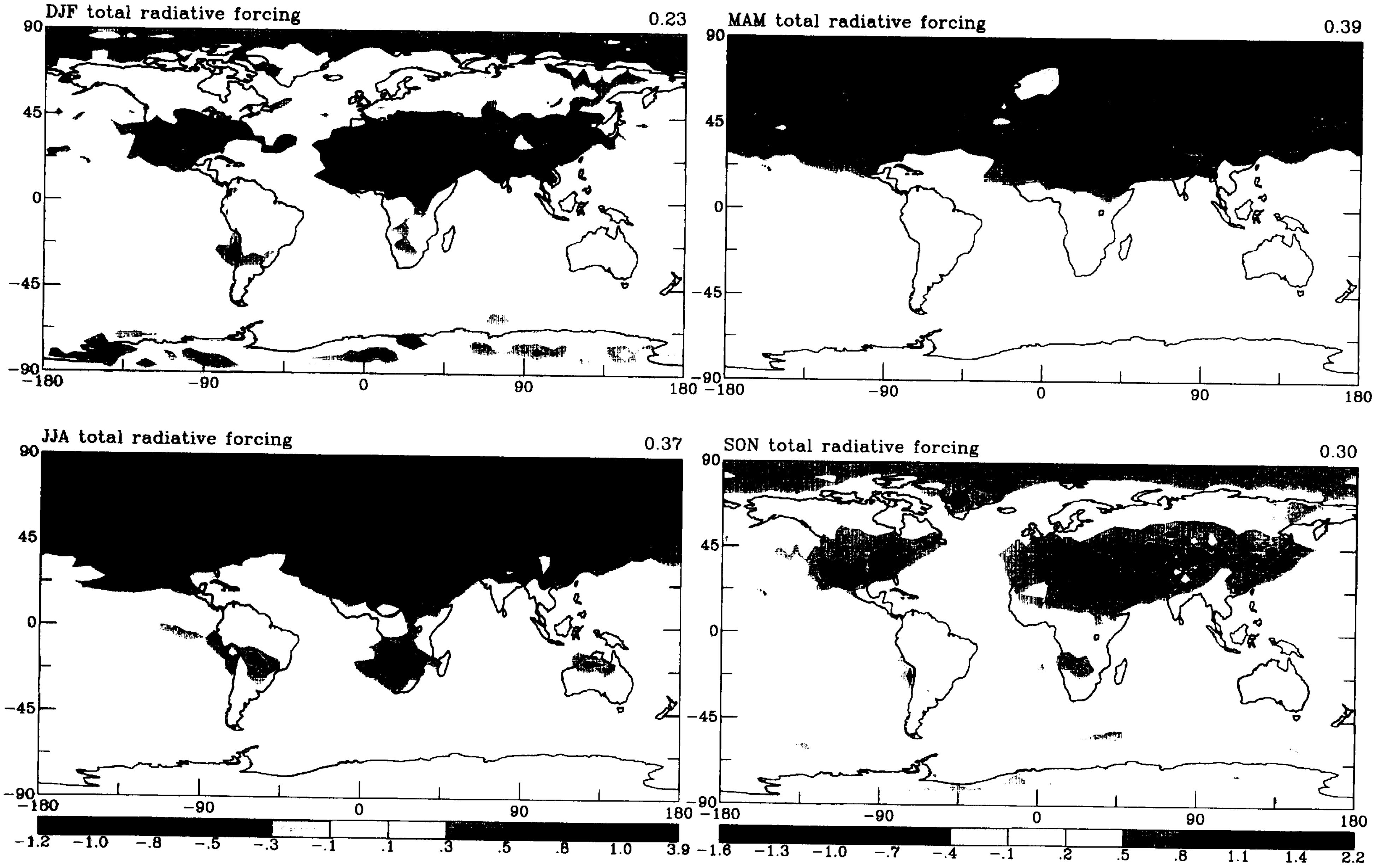
DJF total radiative forcing
0.23
MAM total radiative forcing
0.39
JJA total radiative forcing
0.37
SON total radiative forcing
0.30
90
45
0
-45
-90
-180
-90
0
90
180
-1.2 -1.0 -.8 -.5 -.3 -.1 .1 .3 .5 .8 1.0 3.9
-1.6 -1.3 -1.0 -.7 -.4 -.1 .2 .5 .8 1.1 1.4 2.2

FIG 19

Fig 20

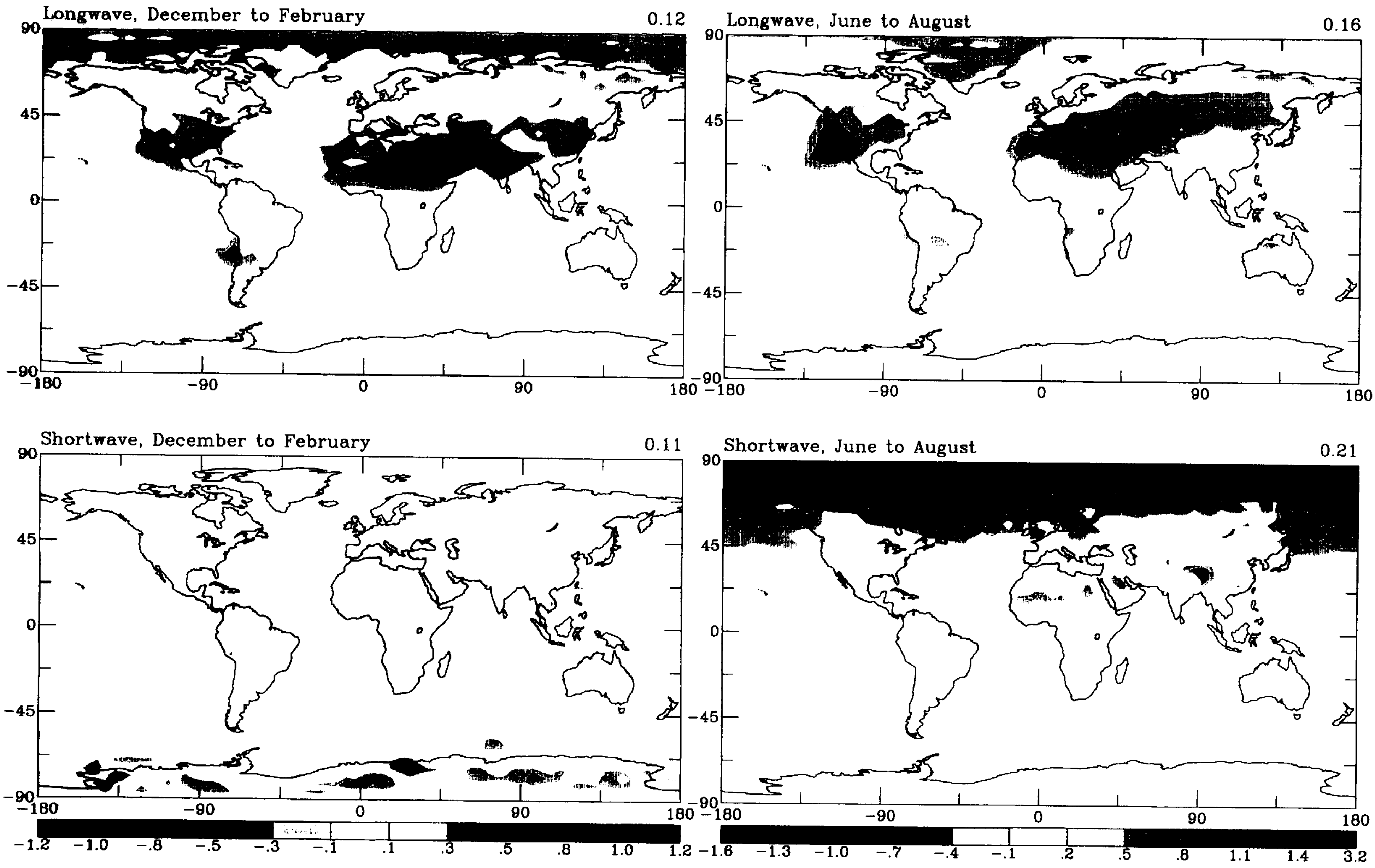
Longwave, December to February
0.12
Longwave, June to August
0.16
Shortwave, December to February
0.11
Shortwave, June to August
0.21
90
45
0
-45
-90
-180
-90
0
90
180
-1.2 -1.0 -.8 -.5 -.3 -.1 .1 .3 .5 .8 1.0 1.2
-1.6 -1.3 -1.0 -.7 -.4 -.1 .2 .5 .8 1.1 1.4 3.2